2015-02-02

Infrared Spectroscopy of C6D6 - Rgn(n=1, 2)

GEORGE, JOBIN

UNIVERSITY OF CALGARY

Infrared Spectroscopy of $C_6D_6 - Rg_n (n = 1, 2)$

by

Jobin George

A THESIS

SUBMITTED TO THE FACULTY OF GRADUATE STUDIES

IN PARTIAL FULFILLMENT OF THE REQUIREMENTS FOR THE

DEGREE OF MASTER OF SCIENCE

DEPARTMENT OF PHYSICS AND ASTRONOMY

CALGARY, ALBERTA

JANUARY, 2015

Abstract

The infrared spectra of $C_6D_6 - Rg_{1,2}$ complexes were observed, with the rare gas (Rg) being He, Ne, Ar. The spectra were observed at a resolution of ~ 60 MHz using a tunable optical parametric oscillator (OPO) to probe a pulsed supersonic-jet expansion from a slit nozzle. The detection system also used a balanced subtraction technique to suppress the power fluctuations inherent to the OPO. Due to a strong Fermi resonance in the C_6D_6 monomer, two bands were observed for each of the complexes, one around the vibrational fundamental of ν_{12} ($\approx$2289 cm^{-1}) and other around the combination band $\nu_2 + \nu_{13}$ ($\approx$2275 cm^{-1}) of the benzene monomer. In the case of C_6D_6−Rg dimers, spectra were assigned to a symmetric top with C_{6v} symmetry with the rare gas atom being located on the C_6 symmetry axis. To observe the C_6D_6−Rg_2 trimers, the nozzle had to be cooled, resulting in spectra with a lower rotational temperature. The spectra of the C_6D_6−Rg_2 trimers were in agreement with a D_{6h} symmetry structure, where the rare gas atoms are positioned on the C_6 symmetry axis, above and below the C_6D_6 plane.

Acknowledgements

I express my deepest appreciation to my supervisor Dr. Nasser Moazzen-Ahmadi for his support, persistent help and guidance that made this thesis possible. His enthusiasm and knowledge of the field have been inspirations to me. Working with him in the lab, I learned the patience and diligence that are necessary for a researcher.

I appreciate the supervisory committee members Dr. David Wesley Hobill, Dr. Brian Jackel and Dr. Yujun Shi for agreeing to review this thesis. I am very grateful to Dr. Jalal Norooz-Oliaee and Dr. Mojtaba Razaei for scientific support and training. My special gratitude towards Dr. Bob McKellar for his valuable contributions to the research presented in this thesis. I am courteous to my supervisor and physics department for financial support.

I thank Sahar Sheybani-Deloui for her comments and feedbacks on the thesis. Also, thanks to my colleagues Mahdi Yousefi Koopaei, Luis Welbanks and Aaron Barclay for their help in the lab and interesting discussions. Gerri, Tracy and Leslie for helping me with the administration processes. Finally, my family for all of their love and support.

Table of Contents

List of Tables

List of Figures and Illustrations

List of Symbols, Abbreviations and Nomenclature

vdW	van der Waals
Rg	Rare gas
He	Helium
Ne	Neon
Ar	Argon
C_6H_6	Benzene
C_6D_6	Deuterated Benzene
ν	Vibrational frequency
Dimer	Two monomer complex
Trimer	Three monomer complex
OPO	Optical Parametric Oscillator
SRO	Singly Resonant Optical parametric oscillator
IR	Infrared
UV	Ultraviolet
N_2O	Nitrous Oxide
N_2	Molecular Nitrogen
CO_2	Carbon Dioxide
TTL	Transistor−transistor Logic
DAQ	Data Acquisition card
PZT	Lead Zirconate Titantate
PPLN	Periodically Poled Lithium Niobate
MgO	Magnesium Oxide
CaF_2	Calcium Fluoride

DFB	Distributed Feedback
PMIFST	Principal Moment of Inertia From Structure
A, B, C	Rotational constants of the molecule
D_{JK}, D_J	Centrifugal distortion constants
ζ	Coriolis coupling constant
Ref.	Reference

Chapter 1

Introduction

In 1873, a modified version of the ideal gas law was proposed by Johannes Diderik van der Waals in order to fit the behaviour of real gases in all temperatures and pressures. The real gases deviate from the ideal gas owing to the finite size of molecules and the intermolecular interaction. The pressure of a gas in a container is lower than the pressure calculated from the ideal gas law due to the intermolecular attraction. All intermolecular interactions are regarded as van der Waals forces. These forces are responsible for bulk properties of simple molecules to complex polymers. Van der Waals forces are responsible for the fundamental properties of matter like melting and boiling points, surface tension, vapour pressure, etc. These forces are also responsible for shapes acquired by synthetic and biological macromolecules. Investigating these forces will shed light into the less understood condensation pathways from molecules in the gas phase to liquid or solid phase. When being cooled down all gases condense to become liquid or solid. The condensation path begins with the formation of molecular clusters, which is simply a finite collection of molecules bound together by van der Waals force.

The molecules involved in the cluster formation can be polar or non polar. There are three types of interactions that are responsible for van der Waals forces. The attractive or repulsive interactions among molecules with permanent dipole moment are called Keesom interactions. A molecule with a permanent dipole moment, otherwise termed as polar molecule can induce a dipole moment on a non-polar molecule. The attractive force between the polar molecule and the non-polar molecule is known as the Debye force (Figure 1.1). The third is the London dispersion force resulting from the attractive force between any molecules (polar or non-polar), where the induced dipole moment of the interacting molecules are instantaneous.

When compared with interatomic bonding (covalent, ionic etc.) the intermolecular forces are very weak, typically of the order of ∼1 kJ/mol, i.e., about two orders of magnitude less than the covalent bond strength.

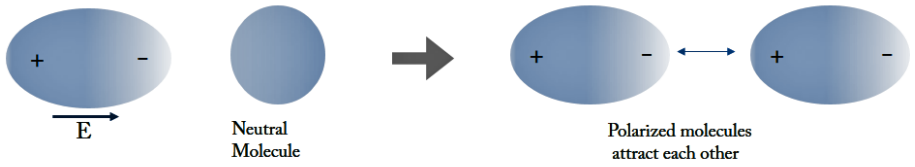

Figure 1.1: Illustration of Debye force, one of three types of van der Waals force between molecules

Our group has been investigating the infrared spectra of weakly bound van der Waals complexes over the past several years. These experimental results are used by theoreticians for modeling potential energy surfaces to obtain information on the intermolecular forces. The experimental results also provide benchmarks for *ab initio* calculations.

A van der Waals bond is characterized by a potential curve with a shallow minimum, since the force is weak, supporting a few vibrational levels. This potential can be approximated by various functions like Lennard-Jones potential or Morse potential. The Lennard-Jones potential is a simple mathematical model for van der Waals interaction, while the Morse potential is a standard potential function used for spectroscopic data analysis. The potential for interaction between two dipoles considering their average angular distribution is inversely proportional to the sixth power of the distance. The potential function consists of an attractive term and a steep repulsive term. Figure 1.2 depicts the potential function for one dimension with a shallow minimum.

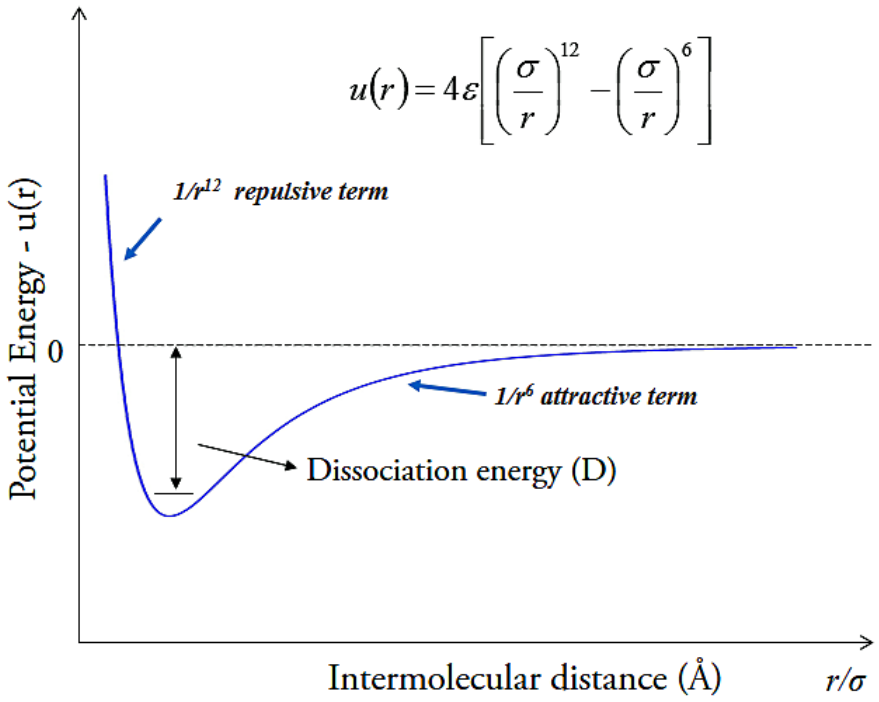

Figure 1.2: Typical Lennard-Jones potential function for a van der Waals bond. Where r is the intermolecular distance, ϵ is the depth of the potential well and σ is the intermolecular separation when $u(r) = 0$

1.1 Generation of van der Waals cluster

The dissociation energy of van der Waals molecules is comparable to the thermal energy at room temperature, k_BT (~2.5 kJ mol^{-1}), hence these molecules readily dissociate. Also, at room temperature molecules typically occupy many thousands of rovibrational states, making spectroscopy challenging. Therefore, a low temperature condition is required for the observation of weakly bound clusters, where the molecules can attain very low rotational temperature.

The supersonic jet expansion technique has been a widely used technique in which the vibrational, rotational and translational cooling of the gas sample is achieved by an adiabatic expansion, where the gas at high pressure is allowed to expand into the vacuum through a pinhole or a slit nozzle. For rotational cooling to occur the pinhole dimension or slit width

must be much larger than the mean free path of the particle in the high pressure region. Consequently, binary collisions of atoms or molecules increases upon entering the vacuum region and internal energy from rotational and vibrational modes is transferred to a large extent into the translational energy. This leads to a decrease in rotational and vibrational temperature, which in turn allows only the lowest ro-vibrational levels of the molecule to be populated. This compression of the population distribution into the lowest levels greatly reduces the number of absorbing states. The drastic reduction in spectral congestion and correspondingly increased signal for the few quantum states which are populated can vastly simplify spectroscopic analysis.

1.2 Observation of van der Waals cluster

A molecule's internal energy is distributed among electronic, vibrational and rotational energy (Figure 1.3). The molecular vibrational energy levels correspond to the mid-infrared(IR) region 2.5-25 μm. Infrared radiation is absorbed when the molecular vibration gives rise to a net change in dipole moment of the molecule. Consequently, absorption at certain frequencies over the bandwidth of the mid-IR source results in an absorption spectrum. It should also be noted that not all transitions are allowed due to a set of selection rules (will be discussed in Chapter 2). When a monochromatic wave of frequency ω and intensity I_0 is passed through a sample of absorption path-length L, the intensity transmitted I_t can be expressed by Beer-Lambert law $I_t = I_0.e^{-\alpha L}$, where α is the absorption coefficient.

Radiation source used in this thesis was a tunable Optical Parametric Oscillator (OPO) which works on the principle of parametric down conversion and has a bandwidth of 1 MHz. To obtain the absorption spectrum, the laser beam is passed perpendicular to the gas flow and where the cluster concentration is the highest. For a single laser pass the sensitivity or signal to noise ratio would not be high enough. To enhance the sensitivity, an astigmatic multi-pass cell is used to make the laser beam pass through the jet around 180 times.

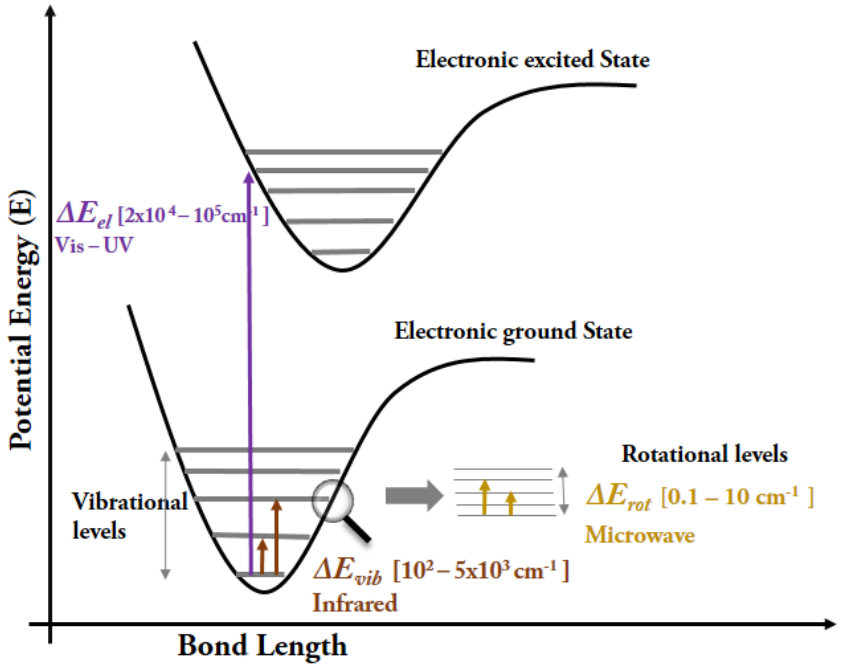

Figure 1.3: Illustration of electronic, vibrational and rotational molecular energy levels and absorption frequencies associated with their transitions.

1.3 Present thesis

The current thesis is concerned with spectroscopic observation and structure determination of Benzene-noble gas complexes. A dimer with one benzene molecule and one noble gas atom and a trimer complex with two noble gas atoms and one benzene molecule were observed and studied. The following sections will explain the motivation behind this study together with a review of previous studies on complexes containing benzene and noble gases.

1.3.1 Benzene-(rare gas)$_n$, n=1,2 complexes

There is a strong interest among researchers to understand the solvation process of molecules through the study of van der Waals complexes. It is the weak van der Waals interactions that lead to solvation phenomena and influence the chemical reactivity in solutions. Organic

molecule - rare gas complexes have been one of the attractive model for studying solvation, thus their spectroscopy at high resolution has an extensive history [11]. The first rotationally resolved spectra of vdW complexes in this class, $C_6H_6 - He$ dimer and $C_6H_6 - (He)_2$ trimer were observed in 1978 by Smalley et al. [14] by means of electronic spectroscopy in a supersonic jet. The resolution of the UV spectrum was very low due to the large laser bandwidth of 1.3 GHz. Only a small number of rotational states were populated due to a low rotational temperature of 0.3 K. Because of the low resolution and a few observed rotational lines, the deduced rotational constants had limited accuracy. However, by assigning the transitions to a symmetric top, the structure of the complexes was estimated as a He atom lying above and/or below the plane of benzene and on the C_6 symmetry axis. A recent study in 2013 by M. Hayashi et al. [17] on the same structure at much higher resolution of $\sim$250 MHz confirmed this structure.

In 1992 Neusser et al. [20] observed the complexes of benzene with other rare gas atoms Ne, Ar, Kr, Xe and also with N_2 molecule. The spectra were obtained with a resolution of 120 MHz. All structures were determined to have the same structure as benzene - He dimer and trimer. Although, the distance between the rare gas atom and the benzene plane differ for each complex due to the variation in polarizability of rare gas atoms [17]. The structures obtained are relatively rigid but when the rare gas atom is replaced with N_2, the structure becomes non rigid because of the internal rotation of the N_2 molecule around the C_6 symmetry axis of the benzene.

Rotational spectroscopy in the microwave region offers much higher resolution, of the order of KHz, and therefore, the structure determined from the deduced rotational parameters is highly accurate. Until 1990 [29], there was no report on the observation of a complex of an aromatic molecule with rare gas atom in the microwave region. This was because the monomers (benzene and rare gas atom) taking part in the formation of the complex have no permanent dipole moment, and the induced dipole moment of the complex is very small

(0.11D). In 1994, Bauder et al. [28] measured the microwave spectra of benzene - Ar and benzene-1,3,5-d_3 - Ar with a resolution of $\sim$ 40 KHz. The isotopic substitution does not change the bond length of the molecules and helps to confirms the structural determination.

So far, there is no observation of benzene - rare gas complexes in the infrared region. This thesis is based on the infrared observation of $C_6D_6 - (Rg)_n$ (n=1,2) with the rare gas being He, Ne, or Ar. The spectra were observed in the regions of ν_{12}, C-D stretch fundamental vibration of C_6D_6 near 2289 cm^{-1} and $\nu_2 + \nu_{13}$ combination band near 2275 cm^{-1} which are coupled by Fermi resonance, where ν_2 is C_6D_6 ring stretch mode and ν_{13} is C_6D_6 ring stretch deformation mode. Fermi resonance is a phenomena in which an overtone or a combination band shows an unexpectedly high intensity. This is discussed in some detail in Chapter 3. For $C_6D_6 - Rg$ dimers, the spectra were assigned to a symmetric top with C_{6v} symmetry with the rare gas atom being located on the C_6 symmetry axis. The $C_6D_6 - (Rg)_2$ trimers were in agreement with a D_{6h} symmetry structure, where the rare gas atoms are positioned above and below the C_6D_6 plane. These structures were already determined using the microwave and electronic spectroscopy [11] except for the $C_6D_6 - (Ne)_2$ trimer. The rotational temperature of trimer spectra were found to be 1.3K. The spectra were observed at a resolution of $\sim$ 60 MHz, which is almost 20 times higher than the first benzene-rare gas complex observation [46].

1.4 Outline of the thesis

The focus of this thesis is on the observation of Benzene-rare gas dimer and trimer complexes in a pulsed supersonic jet apparatus with a continuous wave OPO as probe laser. The thesis has five chapters. Chapter 2 contains an introduction to the theoretical background necessary for the experiment and the analysis of the observed spectrum. The molecular Hamiltonian is introduced and the solutions of the lowest order approximation for rotation-vibration Hamiltonian are presented. The experimental arrangement used for the spectral

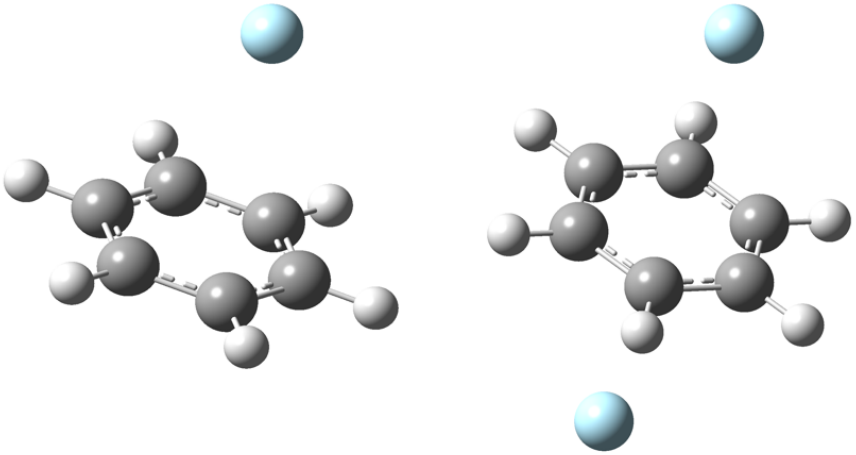

Figure 1.4: Experimentally derived structures of C_6D_6−Rg, C_6D_6−Rg_2 clusters. Rare gas(Rg) in blue is on the C_6 symmetry axis of the Benzene ring

measurement is described in Chapter 3. In this chapter, production of cold molecular beam through supersonic-jet expansion technique, implementation of OPO as probe laser and suppression of power fluctuation is discussed in details. In Chapter 4 the results of the experimental spectra of Benzene-rare gas clusters, the molecular parameters and the corresponding structure of the complexes are presented. Finally, Chapter 5 discuss the conclusion of the experimental studies and future prospectives.

Chapter 2

Theoretical Background

In this chapter, the theory required for analysing the spectroscopic results from the experiment is discussed. The lowest order approximation for the rotational and vibrational Hamiltonian are deduced by modelling the molecule as a combined rigid rotor and harmonic oscillator. The observed van der Waals clusters in this thesis are symmetric top. The rovibrational wavefunctions and energies for rigid symmetric top molecules are presented.

2.1 Molecular Hamiltonian

To treat rovibrational spectra a molecular Hamiltonian must be developed. A molecule is composed of nuclei and electrons that are held together by electrostatic interactions. Thus, the molecular Hamiltonian operator $\hat{H}$ will have the properties of nuclei and electrons. The energies of the molecular system are determined by the eigenvalues of the time-independent Schrödinger equation

$$\hat{H}\Phi = E\Phi, \tag{2.1}$$

where the Hamiltonian $\hat{H}$ can be written as

$$\hat{H} = \hat{T}_{\mathrm{CM}} + \hat{T}_{\mathrm{int}} + \hat{V} + \hat{H}_{\mathrm{es}} + \hat{H}_{\mathrm{hfs}}. \tag{2.2}$$

In Equation 2.2, $\hat{T}_{\mathrm{CM}}$ is the kinetic energy of the center of mass with respect to an arbitrary space fixed system of axes. The second term $\hat{T}_{\mathrm{int}}$ is the sum of the kinetic energy of all particles (electrons and nuclei), which is also the intramolecular kinetic energy with respect to a molecule fixed axes system with the origin at the molecular center of mass. The terms in $\hat{V}$ represent the electrostatic potential energy between the electrons and the nuclei, $\hat{H}_{\mathrm{es}}$ is the interaction energy of the electron spin magnetic moment and $\hat{H}_{\mathrm{hfs}}$ is the interaction due

to the nuclear magnetic and electric moments. In Equation (2.2) one needs to consider only the internal dynamics of the molecule with respect to the molecule fixed axes system. Since any motion with respect to an arbitrary space fixed axes leaves the molecular Hamiltonian invariant. We write 2.2 as

$$\hat{H} = \hat{T}_{\mathrm{CM}} + \hat{H}_{\mathrm{int}} \tag{2.3}$$

$$\hat{H}_{\mathrm{int}} = \hat{H}_{\mathrm{rve}} + \hat{H}_{\mathrm{es}} + \hat{H}_{\mathrm{hfs}} \tag{2.4}$$

where the spin-free rovibronic Hamiltonian $\hat{H}_{\mathrm{rve}}$ is

$$\hat{H}_{\mathrm{rve}} = \hat{T}_{\mathrm{int}} + \hat{V} \tag{2.5}$$

$\hat{H}_{\mathrm{int}}$ can be approximated to $\hat{H}_{\mathrm{rve}}$, for molecules in their singlet electronic ground states with unresolved nuclear hyperfine structure. This approximation is the starting point of any molecular energy calculation. The terms discarded, $\hat{H}_{\mathrm{es}}$ and $\hat{H}_{\mathrm{hfs}}$, are extra terms that give rise to energy level shifts, fine and hyperfine structures. Thus, the rovibronic Schrödinger equation is given by

$$\hat{H}_{\mathrm{rve}}\Psi_{\mathrm{rve}} = E_{\mathrm{rve}}\Psi_{\mathrm{rve}} \tag{2.6}$$

Solving the rovibronic Schrödinger equation (Equation (2.6)) is quite difficult. The direct numerical method would require enormous computational resources. However, it is practical to use indirect methods, which involves making approximations to simplify the Hamiltonian to an extent where the associated Schrödinger equation can be solved rather easily. One of the main approximation among these is the Born-Oppenheimer approximation. This is based on the fact that the electronic motion is so fast in comparison with the nuclear motion that the electronic energy reaches its equilibrium value at each instant. Thus one can treat the vibration and rotation of the nuclei separate from the electronic motion. Thus $\hat{H}_{\mathrm{rve}}$ becomes

$$\hat{H}_{\mathrm{rve}} = \hat{H}_{\mathrm{e}} + \hat{H}_{\mathrm{rv}}. \tag{2.7}$$

As a result, the rovibronic Schrödinger equation is solved by first solving the electronic Schrödinger equation at many fixed geometries and then solving the rotation-vibration

Schrödinger equation for the nuclei. Transitions involved in this thesis are among the rotational-vibrational states in the ground electronic state, so only the rotation-vibration Hamiltonian is considered.

Rigid rotor and harmonic oscillator approximations are made for solving the rotation-vibration Schrödinger equation where the resulting equation is separated into the rotation and vibration parts. Here, the rotational part is the rigid rotor wavefunction expressed in Euler angles whereas the vibrational wavefunction is the product of (3N-6) harmonic oscillator wavefunctions (for linear molecule this is 3N-5), where N is the number of nuclei. For the above approximations it is required to find the appropriate coordinates for the Schrödinger equation. Several coordinate system are introduced for the separation of various molecular motions. The general Hamiltonian in Equation (2.5) is set up in a space fixed axes system, (X, Y, Z). For the separation of rotation and vibration parts of the Schrödinger equation, which enables to understand the rovibrational spectra of a molecule, an axes system (x, y, z) is introduced with the origin at the nuclear center of mass of the molecule. The rovibrational Hamiltonian is then expressed using the coordinates (θ, ϕ, χ) and $(Q_1, Q_2, \ldots, Q_{(3N-6)})$. Where, (θ, ϕ, χ) are the Euler angles which define the orientation of the (x, y, z) axes frame with respect to the (X, Y, Z) axes frame; and the $(Q_1, Q_2, \ldots, Q_{(3N-6)})$ are the normal vibrational coordinates of the molecule.

2.2 Rotation-Vibration Hamiltonian

A detailed derivation procedure of rotation-vibration Hamiltonian is given by Bunker and Jensen [1]. The rovibrational Hamiltonian is expressed in terms of the angular momentum operator $\hat{\boldsymbol{J}}$, normal coordinates $\hat{Q}_r$, their conjugate momenta $\hat{P}_r = -i\hbar\partial/\partial\hat{Q}_r$. With *Born-Oppenheimer* approximation the Hamiltonian is given by

$$\hat{H}_{\mathrm{rv}} = \frac{1}{2}\sum_{\alpha}\mu^{e}_{\alpha\alpha}\hat{J}^{2}_{\alpha} + \frac{1}{2}\sum_{r}^{3N-6}(\hat{P}^{2}_{r} + \omega_{r}\hat{Q}^{2}_{r}), \tag{2.8}$$

$$+ \frac{1}{2}\sum_{\alpha,\beta}(\mu_{\alpha\beta} - \mu^{e}_{\alpha\beta})(\hat{J}_{\alpha} - \hat{p}_{\alpha})(\hat{J}_{\beta} - \hat{p}_{\beta}), \tag{2.9}$$

$$- \sum_{\alpha}\mu^{e}_{\alpha\alpha}\hat{J}_{\alpha}\hat{p}_{\alpha} + \frac{1}{2}\sum_{\alpha}\mu^{e}_{\alpha\alpha}\hat{p}^{2}_{\alpha}, \tag{2.10}$$

$$- \frac{\hbar^{2}}{8}\sum_{\alpha}\mu_{\alpha\alpha} + \frac{1}{6}\sum_{r,s,t}\Phi_{rst}Q_{r}Q_{s}Q_{t} + \frac{1}{24}\sum_{r,s,t,u}\Phi_{rstu}Q_{r}Q_{s}Q_{t}Q_{u} + \cdots . \tag{2.11}$$

where α and β are x, y, and z. $\boldsymbol{\mu}$ is the inverse of the moment of inertia matrix and superscript e stands for a molecule in the equilibrium configuration. $\mu_{\alpha\beta}$ in Equation 2.9 are the elements of $\boldsymbol{\mu}$, which is the inverse matrix of the instantaneous inertia matrix, and $\mu^{e}_{\alpha\beta}$ in Equations 2.8 and 2.10 are the elements of the matrix $\boldsymbol{\mu}^{e}$ which is the inverse of the moment of inertia matrix for the molecule in its equilibrium configuration. $\hat{J}_{\alpha}$ and $\hat{J}_{\beta}$ are referred to as the components of rovibronic angular momentum operators on the molecule's fixed axes, and $\hat{p}_{\alpha}$ and $\hat{p}_{\beta}$ are components of the vibrational angular momentum operator, with $\hat{p}_{\alpha}$ given by

$$\hat{p}_{\alpha} = \sum_{r,s}\zeta^{\alpha}_{r,s}Q_{r}\hat{P}_{s} \tag{2.12}$$

where $\zeta^{\alpha}_{r,s}$ are the Coriolis coupling constants. λ_{r}, Φ_{rst}, and Φ_{rstu} in Equations 2.8 and 2.11 are the terms with force constants which comes from the the Taylor expansion of the potential energy V_{N} in the normal coordinates Q_{r},

$$V_{\mathrm{N}} = \frac{1}{2}\sum_{r}\lambda_{r}Q^{2}_{r} + \frac{1}{6}\sum_{r,s,t}\Phi_{rst}Q_{r}Q_{s}Q_{t} + \frac{1}{24}\sum_{r,s,t,u}\Phi_{rstu}Q_{r}Q_{s}Q_{t}Q_{u} + \cdots . \tag{2.13}$$

and the vibrational kinetic energy operator takes the form

$$\hat{T}_{\mathrm{vib}} = \frac{1}{2}\sum_{r}\hat{P}^{2}_{r} \tag{2.14}$$

The first term of the rovibrational Hamiltonian (Equation 2.8) is the sum of Hamiltonian (H_{rot}) of the rigid rotor and the second term is the sum of $3N-6$ harmonic oscillator Hamiltonians (H_{vib}). The third term (Equation 2.9) is responsible for the centrifugal distortion,

and the terms in Equations 2.10 and 2.11 are due to vibrational Coriolis coupling and anharmonicity, respectively. The anharmonicity results in higher order effects such as Fermi interactions.

2.3 Rigid-Rotor and Harmonic Oscillator Approximation

To solve the rovibrational Schrödinger Equation 2.6, we consider the lowest order of approximation, the rigid rotor approximation in which the molecule is treated as a rigid-rotor and harmonic oscillator approximation where the molecular vibrations is considered as a system composed of $3N-6$ independent harmonic oscillators. Thus we can write approximate rovibronic Hamiltonian as

$$\hat{H}^0_{\mathrm{rv}} = \underbrace{\frac{1}{2}\sum_{\alpha}\mu^e_{\alpha\alpha}\hat{J}^2_{\alpha}}_{\hat{H}_{\mathrm{rot}}} + \underbrace{\sum_{r}^{3N-6}\frac{1}{2}(\hat{P}^2_r + \omega_r\hat{Q}^2_r)}_{\hat{H}_{\mathrm{vib}}} \tag{2.15}$$

and the rotation-vibration Schrödinger equation is

$$\hat{H}^0_{\mathrm{rv}}\Psi^0_{\mathrm{rv}} = E^0_{\mathrm{rv}}\Psi^0_{\mathrm{rv}} \tag{2.16}$$

where Ψ^0_{rv} is the wave functions of the rotation-vibration Hamiltonian given by

$$\Psi^0_{\mathrm{rv}} = \Psi_{\mathrm{rot}}(\theta,\phi,\chi)\underbrace{\Psi_{v_1}(Q_1)\Psi_{v_2}(Q_2)\cdots}_{\Psi_{\mathrm{vib}}(Q_1,Q_2,\cdots,Q_{(3N-6)})} \tag{2.17}$$

and the eigenvalues or energies

$$E^0_{\mathrm{rv}} = E_{\mathrm{rot}} + \underbrace{E_{v_1} + E_{v_2} + \cdots + E_{v_{(3N-6)}}}_{E_{\mathrm{vib}}} \tag{2.18}$$

where

$$[\frac{1}{2}\sum_{\alpha}\mu^e_{\alpha\alpha}\hat{J}^2_{\alpha}]\Psi_{\mathrm{rot}} = E_{\mathrm{rot}}\Psi_{\mathrm{rot}} \tag{2.19}$$

and

$$[\sum_{r}^{3N-6}\frac{1}{2}(\hat{P}^2_r + \lambda_r\hat{Q}^2_r)]\Psi_{v_r} = E_{v_r}\Psi_{v_r} \tag{2.20}$$

Equation 2.19 is the rigid-rotor Schrödinger equation and Equation 2.20 is the harmonic oscillator Schrödinger equations, respectively.

2.3.1 The Principal Moments of Inertia and Rotational Constants

In order to simplify the rotational kinetic energy for the equilibrium nuclear configuration of the molecule we choose the orientation of the molecule fixed (x, y, z) axes as the principal axes of inertia. The moment of inertia matrix $\mathbf{I}$ of a rigid body can be written as

$$\mathbf{I} = \begin{pmatrix} I_{xx} & I_{xy} & I_{xz} \\ I_{yx} & I_{yy} & I_{yz} \\ I_{zx} & I_{zy} & I_{zz} \end{pmatrix} \tag{2.21}$$

where the diagonal elements are

$$I_{\alpha\alpha} = \sum_i m_i(\beta_i^2 + \gamma_i^2) \tag{2.22}$$

where α,β,γ, is a permutation of x, y, z, and m_i are the atomic masses. The off-diagonal elements are

$$I_{\alpha\beta} = -\sum_i m_i \alpha_i \beta_i. \tag{2.23}$$

The rotational Hamiltonian of a molecule is developed in a way that the x, y, z molecule-fixed frame is attached to the molecule so that they align with the principal axes. The x, y, z principal axes makes the off-diagonal elements $I_{\alpha\beta}$ vanish and the diagonal elements are termed as the principal moments of inertia. The principal axes of the equilibrium configuration of molecule are labelled as *a, b* and *c*, the labelling scheme is in the sequence of increasing value of the moment of inertia, i.e.

$$I_a \leq I_b \leq I_c \tag{2.24}$$

Molecules are classified in five groups based on (Equation (2.24)). These are:

- Linear molecule, $I_b = I_c$, $I_a = 0$; example, N_2O.

- Prolate symmetric top, $I_a < I_b = I_c$; example, CH_3Cl.

- Oblate symmetric top, $I_a = I_b < I_c$; example, C_6H_6.

- Spherical top molecule, $I_a = I_b = I_c$; example,CH_4.

- Asymmetric top molecule, $I_a < I_b < I_c$; example, H_2O.

Usually, spectroscopic data are tabulated in units of wavenumber (cm^{-1}). The rigid-rotor Hamiltonian (from Equation 2.15) in cm^{-1} can be written in the principal axes frame (a, b, c) as

$$\hat{H}_{\text{rot}} = \frac{1}{2}\sum_{\alpha} \mu^{e}_{\alpha\alpha}\hat{J}^2_{\alpha} = \hbar^{-2}\left(A\hat{J}^2_x + B\hat{J}^2_y + C\hat{J}^2_z\right) \tag{2.25}$$

where the rotational constants are given by

$$A = \frac{\hbar}{4\pi c I_a},\ B = \frac{\hbar}{4\pi c I_b},\ C = \frac{\hbar}{4\pi c I_c} \tag{2.26}$$

where $\hbar$ is the Planck constant and c is the speed of light. From Equation 2.24 the rotational constants must be in the order of $A \geq B \geq C$. The eigenvalues of the rotational Hamiltonian depend on the rotational constants. The rotational constants depend on the principal moments of inertia, which, in turn depend on the atomic masses, bond angles and bond length of the molecule. Hence, the structure of the molecular system is determined from the rotational constants.

2.3.2 Energy levels and wavefunctions of symmetric top rigid-rotor

The van der Waals complexes observed in this thesis are symmetric top molecular systems, so only energy levels and wavefunctions of the symmetric top molecule are discussed here.

For an oblate top the c-axis is chosen as the z-axis, where the z-axis is the molecular symmetry axis. In the case of prolate tops, the symmetry axis is the a-axis. The commutation relations between $\hat{H}_{\text{rot}}$ and angular momentum operators [13] for an oblate top molecule is given by,

$$[\hat{H}_{\text{rot}}, \hat{J}^2] = [\hat{H}_{\text{rot}}, \hat{J}_Z] = [\hat{H}_{rot}, \hat{J}_c] = 0, \tag{2.27}$$

This implies that $\hat{H}_{\text{rot}}$, $\hat{J}^2$, $\hat{J}_Z$, and $\hat{J}_{a/c}$ share a simultaneous set of eigenfunctions which are represented as $|J, k_c, m\rangle$ for an oblate top and $|J, k_a, m\rangle$ for a prolate top, and the

corresponding eigenvalue equations are

$$\hat{H}_{\text{rot}}|J,k_c,m\rangle = E_{\text{rot}}|J,k_c,m\rangle \tag{2.28}$$

$$\hat{J}^2|J,k_c,m\rangle = J(J+1)|J,k_c,m\rangle \tag{2.29}$$

$$\hat{J}_Z|J,k_c,m\rangle = m|J,k_c,m\rangle \tag{2.30}$$

$$\hat{J}_c|J,k_c,m\rangle = k_c|J,k_c,m\rangle \tag{2.31}$$

where k_c is the quantum number associated with the projection of the total angular momentum onto the molecular fixed axis and the quantum number m is the projection on the symmetry axis fixed in space and it can take the following values,

$$k_c = J, J-1, \ldots, -J+1, -J \tag{2.32}$$

$$m = J, J-1, \ldots, -J+1, -J \tag{2.33}$$

and the eigenfunction

$$|J,k_c,m\rangle = (-1)^{m-k_c}\sqrt{\frac{2J+1}{8\pi^2}}\mathcal{D}^J_{-m,-k_c}(\phi,\theta,\chi). \tag{2.34}$$

$\mathcal{D}^J_{m,k_c}(\phi,\theta,\chi)$ are proportional to the elements of Wigner's rotation matrix, [6], where

$$\mathcal{D}^J_{m,k_c}(\phi,\theta,\chi) = \langle J,m|\mathcal{R}(\phi,\theta,\chi)|J,k_c\rangle, \tag{2.35}$$

where $\mathcal{R}(\phi,\theta,\chi)$ is the rotation operator given by

$$\mathcal{R}(\phi,\theta,\chi) = e^{-i\phi\hat{J}_Z}e^{-i\theta\hat{J}_Y}e^{-i\chi\hat{J}_c}. \tag{2.36}$$

From Equations (2.25) and (2.28) - (2.31), rotational energy levels can be obtained for an oblate top.

$$\hat{H}_{\text{rot}}|J,k_c,m\rangle = \left(A\hat{J}_a^2 + B\hat{J}_b^2 + C\hat{J}_c^2\right)|J,k_c,m\rangle \tag{2.37}$$

$$= \left(A\hat{J}_a^2 - B\hat{J}_c^2 + B\hat{J}_c^2 + B\hat{J}_b^2 + C\hat{J}_c^2\right)|J,k_c,m\rangle \tag{2.38}$$

$$= \left(B\hat{J}^2 + (C-B)\hat{J}_c^2\right)|J,k_c,m\rangle \tag{2.39}$$

Therefore,

$$E_{\text{rot}}(J, k_c) = BJ(J+1) + (C-B)k_c^2. \tag{2.40}$$

Similarly, the energy levels for prolate tops are

$$E_{\text{rot}}(J, k_a) = BJ(J+1) + (A-B)k_a^2. \tag{2.41}$$

From Equation (2.33) it is obvious that for each J value there are $(2J+1)$ different k_c states corresponding to the different possible projections of J on the molecular symmetry axis. Each (J, k_c) level then has $(2J+1)$ different m levels corresponding to projections of J on the space fixed axes. For $k \neq 0$, each level is $2(2J+1)$-fold degenerate since states with $\pm k_a$ having the same energy, whereas the level with $k = 0$ has a degeneracy of $(2J+1)$-fold.

The second term of Equation 2.40 is negative for oblate tops hence the rotational energy decreases with increasing k_c. The wavefunctions of prolate and oblate tops serve as basis function for the asymmetric top molecule.

2.3.3 Harmonic Oscillator Schrödinger Equation

The second term in Equation 2.15 is the vibrational Hamiltonian for N atomic nuclei. The harmonic oscillator Schrödinger equation for the molecular system is

$$[\sum_{r}^{3N-6} \frac{1}{2}(\hat{P}_r^2 + \omega_r \hat{Q}_r^2)]\Psi_v = E_{vr}\Psi_{vr} \tag{2.42}$$

For a single mode of vibration this is

$$\left(\frac{1}{2}(\hat{P}_r^2 + \omega_r \hat{Q}_r^2)\right)\Phi_v(Q_r) = E_v \Phi_v(Q_r) \tag{2.43}$$

where Q is the normal coordinate and $\hat{P}$ the conjugate momentum. The eigenvalues obtained from the above equation is

$$E_v = \left(v + \frac{1}{2}\right)\hbar\omega, \tag{2.44}$$

and the eigenfunctions are

$$\Psi_v = N_v e^{-\omega Q^2/2\hbar} H_v(\sqrt{\frac{\omega}{\hbar}}Q). \tag{2.45}$$

The $H_v(\sqrt{\frac{\omega}{\hbar}}Q)$ is the Hermite polynomial of degree v and N_v is the normalization constant given by

$$N_v = \left(\frac{\sqrt{\omega}}{\sqrt{\hbar\pi}2^v v!}\right)^{\frac{1}{2}}. \tag{2.46}$$

Now, the eigenvalues of Equation 2.42 with all modes of vibration becomes

$$E_{vib} = \sum_{r=1}^{3N-6}\left(v_r + \frac{1}{2}\right)\hbar\omega_r. \tag{2.47}$$

The vibrational eigenfunction for the molecule can be written as the product of the eigenfunctions for each of the normal coordinates,

$$\begin{aligned}\Psi_{vib} &= \Psi_{v_1}(Q_1)\Psi_{v_2}(Q_2)\cdots\Psi_{v_{3N-6}}(Q_{3N-6}) \\ &= \exp\left[-\frac{1}{2}\sum_{r=1}^{3N-6}\frac{\omega_r}{\hbar}Q_r^2\right]\prod_{r}^{3N-6}N_{v_r}H_{v_r}(\sqrt{\frac{\omega_r}{\hbar}}Q_r),\end{aligned} \tag{2.48}$$

Based on the degeneracies of the normal modes, the complete vibrational wavefunctions of a molecule is written as a product of one-, two- or three- dimensional harmonic oscillator functions.

Anharmonicity

The experimental studies of molecular spectra and calculations on simple molecular systems have shown that the general vibration potential function is anharmonic in nature. The harmonic oscillator model does not include the anharmonicity and the dissociation limit. Morse potential function is a practical function used for simulating the vibrations between two nuclei in a molecule. Morse potential includes anharmonicity and at larger internuclear distance, it asymptotically approaches a dissociation limit. Figure 2.1 shows the vibrational energy levels for the first few levels of Harmonic oscillator and Morse Potential. The anharmonicity effects becomes significant for higher vibrational quantum number.

$$V_v(r) = D\left(1 - e^{-\alpha(r-r_e)}\right)^2. \tag{2.49}$$

where D is the dissociation energy of the molecule, r_e is the equilibrium nuclear distance. Taking into account the cubic term in the expansion of the potential function the vibrational

energy is given by,

$$E_{vib}(v) = \omega_e(v + \frac{1}{2}) - \omega_e\chi_e(v + \frac{1}{2})^2. \tag{2.50}$$

There are higher order terms, which will not be discussed here.

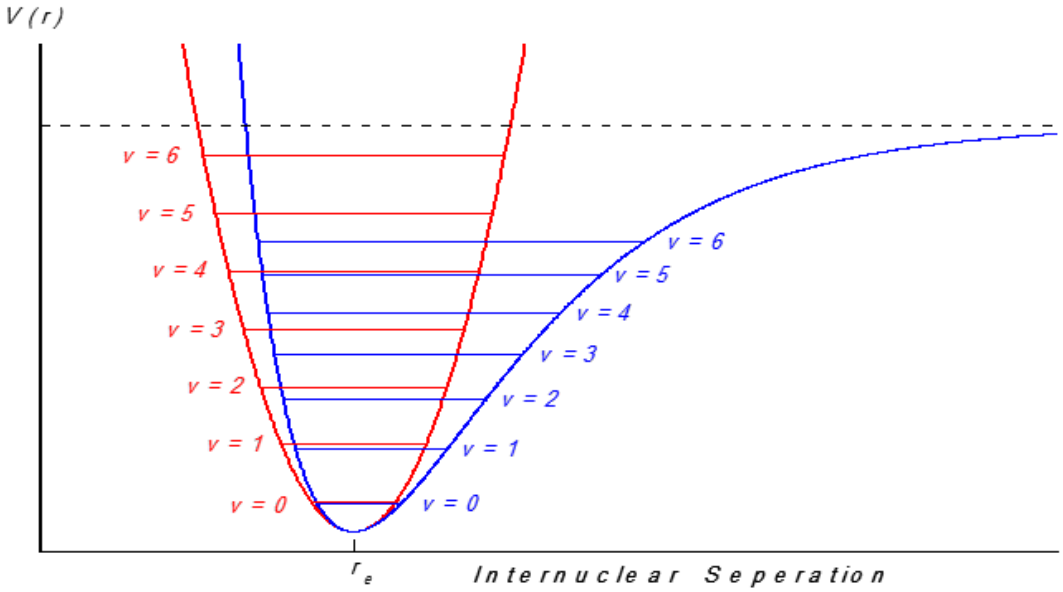

Figure 2.1: Figure shows few vibrational levels of the harmonic potential (red trace) and Morse potential (blue). The anharmonicity is taken into account in the realistic Morse potential. The units are arbitrary

2.4 Centrifugal Distortion

So far, we approximated the molecules as rigid, but in reality a molecule is not strictly rigid. As a non rigid rotating body the atoms in molecules experience centrifugal force. This leads to a slight change in the moment of inertia of the molecule. The centrifugal distortion constants are corrections to the rotational constants. Thus, the centrifugal distortion constants possess information about bond strengths within the molecule.

Taking into account the diagonal centrifugal distortion constants, the energy expression

for a prolate top becomes

$$E_{\rm rot}(J,k_c) = BJ(J+1) + (C-B)k_c^2 - D_J[J(J+1)]^2 - D_{JK}J(J+1)k_c^2 - D_K k_c^4, \quad (2.51)$$

where D_J, D_{JK} and D_K are distortion constants of order B^2/ω, ω is the molecular vibrational frequency. The values of distortion constants are many orders of magnitude smaller than the rotational constants B and C. The frequency for an R-branch transition $J \rightarrow J+1$, $\triangle K = 0$ is given by

$$\begin{aligned} \nu &= E_{\rm rot}(J+1,K) - E_{\rm rot}(J,K) \\ &= 2(B - D_{JK}k_c^2)(J+1) - 4D_J(J+1)^3 \end{aligned} \quad (2.52)$$

where K is the absolute value of k_c. In the absence of centrifugal distortions, rotational transitions are equally spaced and for a given lower state value of J all transitions with different values of K have identical frequencies. For pure rotational transitions the selection rule is $\Delta K = 0$, K dependent terms in Equation 2.51 disappears, it is therefore not possible to determine the A or C constants. For the rovibrational transitions with the selection rule $\Delta K = \pm 1$ (Section 2.6), it is possible to determine A or C in the ground or excited state.

2.5 Coriolis Coupling

The Coriolis forces are responsible for the coupling of different normal vibrational modes via a rotational degree of freedom. The Coriolis coupling can also occur between the components of the degenerate vibrational mode, for example coupling of degenerate C-H stretching modes in benzene [8]. In the lowest order, the degenerate vibrational modes are treated as a two-dimensional isotropic harmonic oscillator, with the energy of the mode given by $E_v = (v+1)\hbar\omega$.

Because the motion of the atoms in a degenerate vibrational mode is perpendicular to the molecular axis, the vibrational angular momentum $p_v = \zeta_v l_v$ generated is along the molecular axis, where l_v, the vibrational angular momentum quantum number, can have

values between v to $-v$ in steps of 2 and $|\zeta|$ is the coupling constant which varies between 0 and 1. Taking into account the vibrational angular momentum, the quadratic part of the rotational Hamiltonian of the symmetric top becomes [7]

$$\hat{H_{\text{rot}}} = B(\hat{J}_x^2 + \hat{J}_y^2) + C(\hat{J}_z^2 - p_v)^2 \tag{2.53}$$

Substituting for p_v and expanding the above equation, we get

$$\hat{H}_{\text{rot}} = B(\hat{J}_x^2 + \hat{J}_y^2) + C\hat{J}_z^2 - 2C\hat{J}_z\zeta_v l_v = (C-B)\hat{J}_z^2 + B\hat{J}^2 - 2C\hat{J}_z\zeta_v l_v \tag{2.54}$$

where the term $C(\zeta_v l_v)^2$ is neglected, since it is purely vibrational and does not affect the rotational state. Now, the energies of the Hamiltonian is given by,

$$E_{rot} = BJ(J+1) + (B-C)k_c^2 - 2Ck_c\zeta l_v \tag{2.55}$$

where the term $2Ck_c\zeta l_v$ represents the contribution of the Coriolis coupling. The Coriolis coupling splits the energy levels, since k and l can take positive or negative values in Equation 2.55.

There is also a small but measurable contribution from the higher order terms in the rovibrational Hamiltonian. The most important among these is referred to as l-doubling, which is due to the operator given by,

$$\hat{H}_{\text{ld}} = \frac{1}{4}q_v\left(\hat{J}_+^2 q_{v-}^2 + \hat{J}_-^2 q_{v+}^2\right) \tag{2.56}$$

where $\hat{J}_\pm = \hat{J}_x \pm i\hat{J}_y$ and $q_{v\pm} = q_{v,a} \pm iq_{v,b}$ are ladder operators, subscripts a and b indicate the two components of the degenerate mode. The first term in Equation 2.56 lowers the k and l_v quantum number by 2 and the second term raises both quantum numbers by 2. The coupling of the degenerate vibrational modes occurs in the same plane.

2.6 Absorption line Intensities and Selection rules

Consider a monochromatic radiation with an intensity I_0 and wavenumber $\tilde{\nu}$ travelling a distance l through a sample with concentration c^*. The transmitted intensity according to

the Beer-Lambert law is given by,

$$I(\tilde{\nu}) = I_0(\tilde{\nu})e^{-lc^*\sigma(\tilde{\nu})} \tag{2.57}$$

where $\sigma(\tilde{\nu})$ is the absorption coefficient. The absorption coefficient is a measure of the extent to which the initial intensity is absorbed. Molecules absorb or emit infrared radiation when the vibration of the molecule give rises to a change in the electric dipole moment, μ.

Considering that molecules are in thermal equilibrium at an absolute temperature of T, the intensity of an absorption line is proportional to the fraction of the molecules $F(E_i)$ in the initial energy state E_i. From *Maxwell- Boltzmann Distribution*,

$$\text{Fraction of molecules in level } E_i: \ F(E_i) = \frac{g_i e^{-E_i/k_B T}}{\sum_j g_j e^{-E_j/k_B T}}, \tag{2.58}$$

where k_B is the Boltzmann constant, g_i is the degeneracy of the state i. $F(E_i)$ varies with temperature and a sample at a very low temperature has only few of the lowest energy levels of the molecules are populated hence the spectrum appears much simpler than a sample at a higher temperature.

Apart from the absorption of radiation, molecules also undergo resonant stimulated emission. In stimulated emission, a molecule in an excited energy state E_f is stimulated by a radiation of frequency ν_{if} to drop into a lower energy state of E_i. This process reduces the absorption process by a multiplicative factor given by [3],

$$\text{Resonant stimulated emission}: \ R_{\text{stim}}(f \longrightarrow i) = 1 - \exp\left(-h\tilde{\nu}_{if}/k_B T\right) \tag{2.59}$$

In addition to the population of the initial state and stimulated emission, the spectral line intensity also depends on an intrinsic value called the line strength $S(f \longleftarrow i)$. The line strength depends on the molecular electric dipole moment for the transition between rotational levels and the change in the electric dipole moment for the transition between vibrational levels.The integrated absorption coefficient for an electric dipole transition between states with initial energy of E_i and final energy of E_f, is given by [1]

$$I(f \longleftarrow i) = \int_{Line} \sigma(\tilde{\nu}) d\tilde{\nu} \tag{2.60}$$

$$= \frac{8\pi^3 N_A \tilde{\nu}_{if}}{(4\pi\epsilon_0)\, 3hc^2} F(E_i) R_{\text{stim}}(f \longrightarrow i) S(f \longleftarrow i) \tag{2.61}$$

where N_A is the Avogadro number, $\tilde{\nu}_{if} = (E_f - E_i)/hc$ is the frequency of the transition in cm^{-1}, h is the Planck's constant, c is the speed of light in vacuum, ϵ_0 is the permittivity of vacuum, and function $S(f \longleftarrow i)$ is

$$\text{Line strength}: \; S(f \longleftarrow i) = \sum_{A=X,Y,Z} |\langle \Psi' | \mu_A | \Psi \rangle|^2, \tag{2.62}$$

where μ_A $(A = X, Y, Z)$ are the components of the electric dipole moment in the space-fixed axis and Ψ' and Ψ are eigenfunctions of the molecular Hamiltonian. Let us express μ_A in terms of the components of electric dipole moment in the molecule-fixed frame

$$\mu_A = \sum_{\alpha=x,y,z} \lambda_{A_\alpha} \mu_\alpha \tag{2.63}$$

here λ represents the transformation matrix from space fixed to molecular fixed frame, whose elements are functions of Euler angles, and μ_α is given by

$$\mu_\alpha = \sum_j e_j q_{\alpha j}, \tag{2.64}$$

where $q_{\alpha j}$ and e_j is the coordinate and the charge of the jth particle. The Taylor expansion series of μ_α about the equilibrium configuration of the molecule can be written as

$$\mu_\alpha = \mu_\alpha^0 + \sum_{l,k} \left(\frac{\partial \mu_\alpha}{\partial q_{\alpha l}} \right)_0 q_{\alpha l} + \frac{1}{2} \sum_{l,k} \left(\frac{\partial^2 \mu_\alpha}{\partial q_{\alpha l} \partial q_{\alpha k}} \right)_0 q_{\alpha l} q_{\alpha k} + \cdots . \tag{2.65}$$

Considering only rovibrational transitions within a given electronic state, the $|\Psi\rangle$ can be taken as the product of $|\Psi_v\rangle$(vibrational) and $|\Psi_{rot}\rangle$(rotational) wavefunctions. The integral in Equation 2.62 becomes

$$\langle \psi_v' \psi_{rot}' | \mu_A | \psi_v \psi_{rot} \rangle = \overbrace{\sum_\alpha \langle \psi_v' | \psi_v \rangle \langle \psi_{rot}' | \lambda_{A\alpha} | \psi_{rot} \rangle \mu_\alpha^0}^{\text{Pure rotational}}$$

$$+\overbrace{\sum_{\alpha}\sum_{l,k}\left(\frac{\partial\mu_{\alpha}}{\partial q_{\alpha l}}\right)_0\langle\psi'_{rot}|\lambda_{A\alpha}|\psi_{rot}\rangle\langle\psi'_{v}|q_{\alpha l}|\psi_{v}\rangle}^{\text{Rovibrational}}$$

$$+\overbrace{\sum_{\alpha}\sum_{l,k}\left(\frac{\partial^2\mu_{\alpha}}{\partial q_{\alpha l}\partial q_{\alpha k}}\right)_0\langle\psi'_{rot}|\lambda_{A\alpha}|\psi_{rot}\rangle\langle\psi'_{v}|q_{\alpha l}q_{\alpha k}|\psi_{v}\rangle}^{\text{Combination and overtones}}$$

$$+\cdots. \tag{2.66}$$

The possibility of a transition between any two energy levels is determined by the integrals in each term of Equation 2.66.

Rotational selection rule

For a given vibrational state, $\langle\Psi'_v|\Psi_v\rangle = 1$, hence pure rotational transitions within a given vibrational level are governed by the term $\langle\Psi'_{rot}|\lambda_{A\alpha}|\Psi_{rot}\rangle$ in Equation 2.66. With a permanent dipole moment, i.e. $\mu_{\alpha}^{eq} \neq 0$, the rotational matrix elements are

$$\langle\Psi'_{\rm rot}|\lambda_{A_\alpha}|\Psi_{\rm rot}\rangle = \langle J', k', m'|\lambda_{A_\alpha}|J, k, m\rangle \tag{2.67}$$

For example, for symmetric top molecules the selection rules for the quantum numbers J, k, and m in Equation (2.67) are

$$\Delta J = \pm 1, \quad \Delta m = 0, \pm 1, \quad \Delta k = 0. \tag{2.68}$$

Rovibrational transitions

The second term in equation 2.66 dictates the rotational transitions between different vibrational levels which is relevant for the fundamental vibrations studied in this thesis. The vibrational matrix elements $\langle\Psi_{v'}|q_{\alpha l}|\Phi_v\rangle$ gives the vibrational selection rules and the rotational matrix elements $\langle\Psi'_{rot}|\lambda_{A_\alpha}|\Psi_{rot}\rangle$ determine the rotational selection rules. Considering a symmetric top molecule as an example, there are two kinds of allowed transitions:

(i) **Parallel bands:** If the transition moment of the vibrational transition is parallel to the symmetric top axis or z-axis, the selection rules for the vibrational

and rotational quantum numbers are

$$\Delta v = \pm 1, \quad \Delta J = 0, \pm 1, \quad \Delta k = 0 \quad \text{if} \quad k \neq 0,$$
$$\Delta v = \pm 1, \quad \Delta J = \pm 1, \quad \Delta k = 0 \quad \text{if} \quad k = 0. \tag{2.69}$$

(ii) **Perpendicular bands:** The electric dipole moment variation is in the direction perpendicular to the top axis and the selection rules are

$$\Delta v = \pm 1, \quad \Delta J = 0, \pm 1, \quad \Delta k = \pm 1. \tag{2.70}$$

Combinations and overtones

The third term and higher orders terms in Equation 2.66 are responsible for the combination and overtone bands. Since higher derivatives of the dipole moment are much smaller than the first derivative, these bands are normally very weak.

$$\partial^2 \mu / \partial Q^2 \sim 0.01 \mu \tag{2.71}$$

Typically, combination bands are 50 to 100 times weaker than the fundamental bands.

2.6.1 Nuclear spin statistical weights

The existence of nuclear spin affects the population of rotational levels, which explains certain intensity patterns. For example, molecules with centre of symmetry like CO_2, the odd-J rotational lines in P and R branch have zero intensity. So finding a statistical weight of the rovibronic states is necessary for assigning molecular spectra.

The complete internal wavefunction of the molecule Ψ_{int} is the product of rovibronic wavefunction Ψ_{rve} and the nuclear spin wavefunction Ψ_{ns}. A rovibronic state would be populated (have non zero statistical weight) only if the product of the symmetries of the Ψ_{rve} and Ψ_{ns} is an allowed symmetry in Ψ_{int}. This product forms a basis function for expressing Ψ_{int}.

From the Fermi-Dirac and Bose-Einstein statistics, the complete internal wavefunctions Ψ_{int} of the molecule must be invariant under even or odd permutations of bosons (integer spin) and any even permutation of identical fermions (half integer spin). This means that sign of Ψ_{int} will change only under an odd permutation of identical fermions. These can be written as,

$$P_{(even)}\Psi_{int} = \Psi_{int}, \qquad P_{(odd)}\Psi_{int} = -\Psi_{int} \qquad \text{for fermions,} \tag{2.72}$$

$$P_{(even/odd)}\Psi_{int} = \Psi_{int} \qquad \text{for bosons.} \tag{2.73}$$

In addition to this Ψ_{int} can have + or - parity due to the effect of inversion operation E^*. E^* is defined as, when applied to a molecule, the operation of inverting the spatial coordinates of all the nuclei.

$$E^*\Psi_{int} = \pm\Psi_{int}. \tag{2.74}$$

Using Equations (2.72) and (2.74), the symmetry of the complete internal wavefunction can be determined. To form an acceptable basis function for Ψ_{int}, the product of the symmetry species of rovibronic state and the nuclear spin state must contain the symmetry species for Ψ_{int}. This condition explains the missing of certain spectral lines and different statistical weights for various rovibronic states which give rise to intensity alternations.

2.7 Fermi Resonance

The rotation-vibration Hamiltonian Equations 2.9 to 2.11 shows the terms that introduce perturbations within an electronic state. These terms are responsible for the interaction between states that are in resonance (having energies that are close). The perturbations caused by anharmonicity are introduced by cubic, quartic, quintic, ..., terms in the expansion of the potential energy (Equation 2.13). Among these, the cubic potential energy term gives rise to the interaction between the fundamental vibration and overtone or combination states. This interaction results in frequency shifts and stealing of intensity from the strong

fundamental band to overtone or combination band, the phenomenon is referred as Fermi resonance. The observation of Fermi resonance is of particular interest in the thesis and is discussed in the next chapter. When the resonating levels are close in energy, the magnitude of the energy shift can be obtained. For two resonating levels a and b, the shifted energy λ is given by the determinant, [4]

$$\begin{vmatrix} E_a^0 - \lambda & H' \\ H' & E_b^0 - \lambda \end{vmatrix} = 0, \tag{2.75}$$

where H' is the off diagonal Fermi coupling constant term. The solution of the equation 2.75 is given by,

$$\lambda = \frac{E_a^0 + E_b^0}{2} \pm \frac{1}{2}[4 \mid H' \mid^2 + (E_a^0 - E_b^0)^2]^{1/2} \tag{2.76}$$

$E_a^0 - E_b^0$ is the energy separation of the unperturbed levels. The first term gives the mean energy of the levels. The second term shows that one level is pushed up in energy and the other down.

In C_6D_6, the combination mode (ν_2+ν_{13}) and the fundamental mode (ν_{12}) have nearly the same frequency and are of same symmetry, hence they interact strongly by Fermi resonance. The cubic potential term in the the Hamiltonian that causes this interaction is,

$$\mathrm{H}' = \frac{1}{2}\mathrm{K}_{2,12,13}\mathrm{Q}_2\mathrm{Q}_{12}\mathrm{Q}_{13} \tag{2.77}$$

where $K_{2,12,13}$ is the cubic potential constant. Q_2, Q_{12} and Q_{13} are the corresponding vibrational coordinates. For C_6D_6, the shift due to Fermi resonance between combination mode ($\nu_2 + \nu_{13}$) and the fundamental mode (ν_{12}) in equation 2.76 is about $\sim -3.9\mathrm{cm}^{-1}$.

Chapter 3

Experimental Set-up

3.1 A Brief Description of the Experimental Set-up

In this chapter the experimental set-up used to record the spectra is discussed in detail. Figure 3.1 shows a schematic of the experimental arrangement. Some of the main components of the system are the supersonic jet expansion, IR laser source, IR detectors, the multipass cell, transfer optics and the data acquisition. The clusters were generated by a single pulsed nozzle in a supersonic expansion and were probed using the laser source. The signal to noise ratio of the absorption spectra is increased by increasing the laser path length through the supersonic jet. This is done by employing a multipass cell in the vacuum chamber. To calibrate the observed spectra in frequency, an absorption spectrum of a reference gas at room temperature and an etalon, with a free spectral range(FSR) of 285 MHz (0.0099 cm^{-1}) were used. The signals from the jet, reference gas and etalon were recorded.

The following sections will describe the supersonic jet expansion and multipass cell, Optical Parametric Oscillator and its working principle, and then a detailed discussion of transfer optics and data acquisition scheme is given.

3.2 Supersonic Jet Expansion

Supersonic jet expansion can provide an almost perfect sample suitable for spectroscopic studies. The adiabatic jet expansion creates a low temperature environment. The low temperature is important because (a) it is essential for creating weakly bound van der Waals clusters which would otherwise dissociate at higher temperature and (b) spectra obtained are simplified because only the lowest rotational levels in the ground vibrational state are

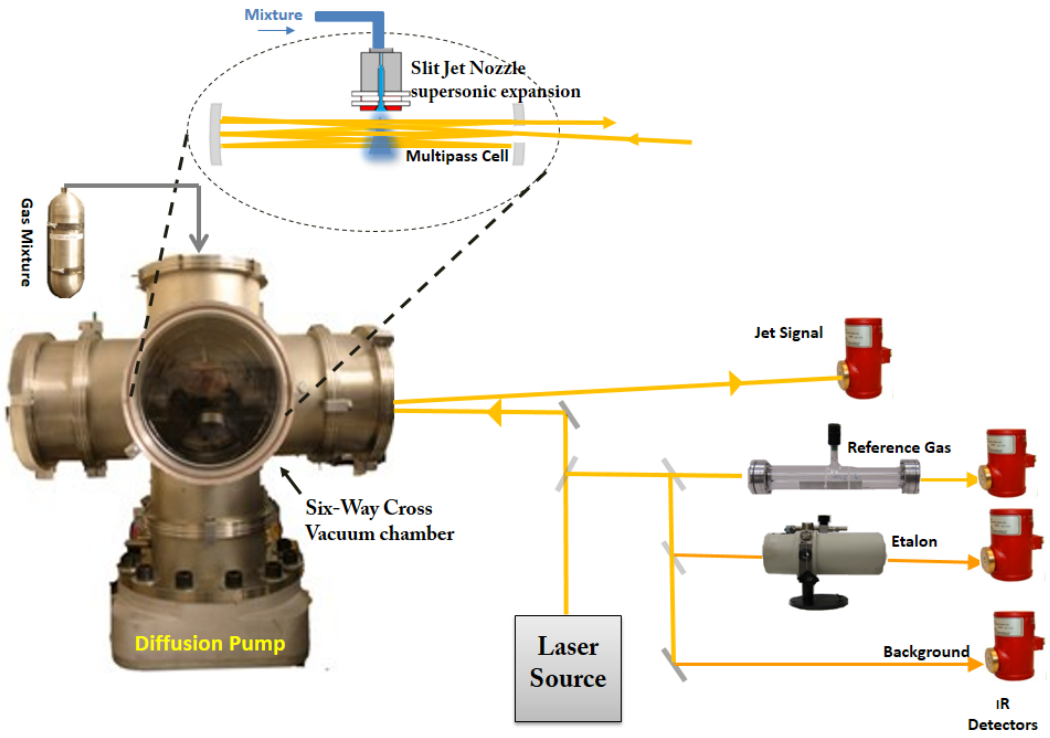

Figure 3.1: Schematic of the experimental set-up for van der Waal cluster spectroscopy. Probe beam is separated into four channels: jet, reference gas, etalon and a fourth channel for background. Jet signal records the absorption spectra of clusters. All channels are recorded simultaneously. The astigmatic multipass cell increases the effective optical path length of the probe laser beam through the supersonic cluster stream, hence enhances the signal-to-noise ratio.

populated and this in turn simplifies the spectral analysis. High collimation and collision free molecular jet beam eliminates pressure broadening and significantly reduces Doppler broadening.

Although the cooling process is complicated, the best way of understanding the process is as follows. The supersonic jet expansion occurs so fast that heat exchange of the gas with its surrounding is insignificant and the expansion can be taken as an adiabatic process. From the conservation of energy, it is required that the total energy before and after the expansion to be the same. Consider a mole of gas being expanded from a high pressure reservoir with pressure P_0 and volume V_0 to a low pressure (P) region of volume V. The total energy before

and after the expansion can expressed as,

$$\underbrace{U_0 + P_0V_0 + \frac{1}{2}mu_0^2}_{\text{before expansion}} = \underbrace{U + PV + \frac{1}{2}mu^2}_{\text{after expansion}} \tag{3.1}$$

where, $\frac{1}{2}mu^2$ is its kinetic energy of the expanding gas, $U = U_{\text{tr}} + U_{\text{v}} + U_{\text{r}}$ is its internal energy which comprises of the translational (U_{tr}), vibrational (U_{v}) and rotational energy (U_{r}), and PV is its potential energy. Considering the reservoir is in thermal equilibrium, the average velocity of all the gas molecules u_0 is zero. Hence, the kinetic energy of the gas before the expansion can be neglected. Since, the gas expands into a vacuum, the pressure P after the expansion is very small. Thus, the potential energy PV of the expanded gas can also be neglected. We therefore get,

$$U_0 + P_0V_0 = U + \frac{1}{2}mu^2 \tag{3.2}$$

$$U_0 - U = \frac{1}{2}mu^2 - P_0V_0 = \frac{f}{2}k_B(T_0 - T) \tag{3.3}$$

where f is the number of degrees of freedom, k_B is the Bolzmann constant, T_0 and T is the temperature before and after the expansion. From Equation 3.3 we conclude that a significant amount of internal energy before the expansion converts into the kinetic energy of the gas flow, which becomes possible due to a large number of collisions in the initial stages of the expansion. The non zero average velocity after the expansion accounts the directional kinetic energy. The significant decrease in internal energy also corresponds to the large decrease of temperature.

3.2.1 Description of supersonic jet expansion

As mentioned earlier, in a supersonic jet expansion the stream of gas is allowed to expand from a high pressure region into the vacuum through a nozzle (Figure 3.2). This is supersonic since the speed of gas stream surpasses the local speed of sound during expansion. Before the expansion, the gas is in thermal equilibrium and velocity distribution of the gas obeys

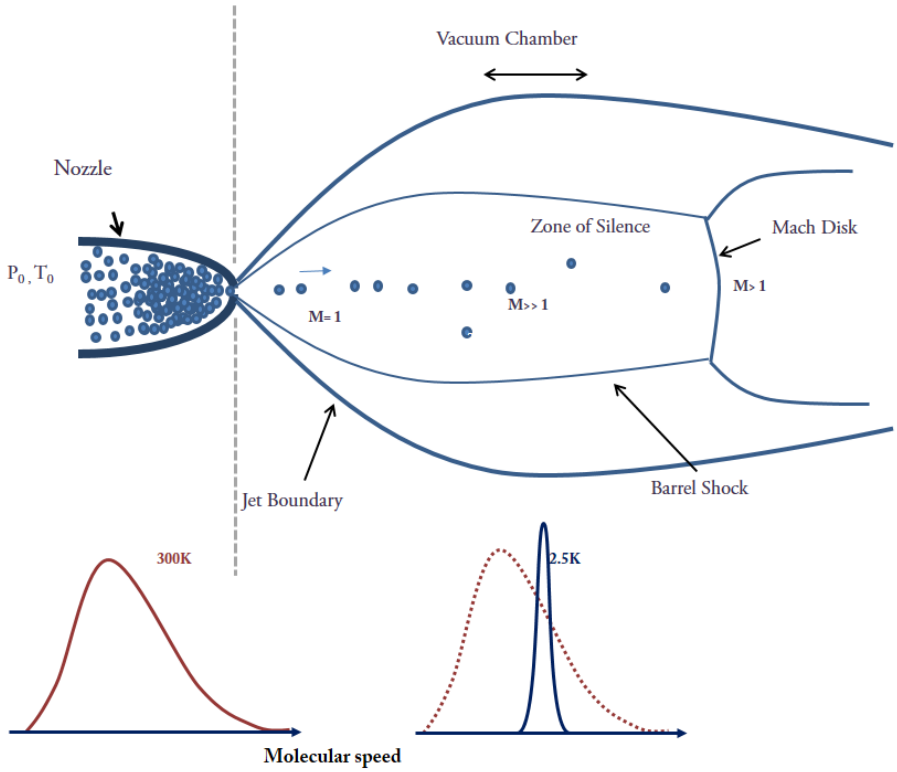

Figure 3.2: Illustration of the supersonic jet expansion of the gas from a nozzle. High pressure inside the reservoir gives rise to many collisions near the nozzle opening during the expansion. Consequently these collisions transfer momentum into the direction downstream. The zone of silence is the collision free region, the mach disk is shock front perpendicular to the flow. The velocity distribution before and after the expansion is shown at the bottom of the figure

Maxwell-Boltzmann distribution. from Equation 3.3 it is evident that during the expansion the thermal energy is converted into directional kinetic energy and this decreases the temperature of the jet progressively. As shown in Figure 3.2 the collisions and the relative velocity tend to decrease and the atomic velocity distribution gets narrower and narrower. Note that more than 99% of the gas mixture is composed of Helium, the seeded molecular sample is less than 1%. This is because the rare gas molecules like Helium have no internal degrees of freedom like rotation and vibration, so the energy associated with the internal degrees of polyatomic molecules can be efficiently transferred to rare gas molecules.

For an ideal gas expanding adiabatically in reversible conditions, an isentropic equation

of state can be used to describe the temperature, pressure and density of the beam as a function of the scale of the expansion [15] [9].

$$\frac{T}{T_0} = \left(\frac{P}{P_0}\right)^{\frac{\gamma-1}{\gamma}} = \left(\frac{\rho}{\rho_0}\right)^{\gamma-1} = \frac{1}{1+\frac{(\gamma-1)}{2}M^2} \tag{3.4}$$

where T_0, P_0 and ρ_0 are the temperature, pressure and density before expansion in the reservoir; T, P and ρ are the same quantities during the expansion; γ is the ratio of the heat capacity $\frac{C_p}{C_v}$, C_p is the specific heat of ideal gas at constant pressure, C_v is the specific heat at constant volume and M is the Mach number which is the ratio of molecular beam velocity and the local speed of sound. It is evident from the Equation 3.4 that as the Mach number increases the temperature, pressure and density decrease with the expansion from the orifice. The increase in Mach number is the result of the conversion of thermal energy into directed kinetic flow. Collisions among the molecules are necessary for this process. With increasing distance from the nozzle the collision frequency decreases and the jet density and the temperature decreases. Thus the Mach number provides a measure of the local temperature of the jet [18]. As the collisions decrease with density the Mach number reaches a finite value, M_T, the terminal Mach number for argon as given by Smalley et al. [15] is,

$$M_T = 133(P_0 D)^{0.4} \tag{3.5}$$

where P_0 is the reservoir chamber pressure, D is the diameter of the nozzle. The P_0D in Equation 3.5 simply describes the terminal Mach number is proportional to number of two body collisions. To increase the number of collisions thereby increasing the extent of cooling, the pressure in the reservoir should be high enough so that D>> λ_0, where λ_0 is the mean free path of the gas. In a supersonic expansion the translational temperature can reach as low as 1 K. Usually, the order of vibrational temperature in supersonic expansion is 20 âĹŠ 150 K and rotational temperature from 1 to 10 K.

3.2.2 Cluster formation in supersonic jet

In a supersonic expansion process, two-body collisions narrow down the velocity distribution of the gas particles and thereby are responsible for cooling. But, the cluster formation is favoured by three-body collisions. When atoms or molecules approach each other, they bind together and the energy released is transferred to a third body by collision which stabilizes the cluster. It has been shown that the two-body and three-body collisions are proportional to P_0D and P_0^2D [15], so increasing gas reservoir pressure favours the formation of larger clusters. Typical reservoir pressure used in our system were between 7 to 14 atm. Specially designed nozzles, such as slit nozzles, which makes the expansion slower is also utilized to increase the cluster population. [40, 41].

Slit shaped nozzles forms planar supersonic expansion with the jet velocity in the plane of the slit downstream. Slit nozzles give longer optical absorption path length and also result in higher cluster number density. Highly collimated jet velocity and very narrow velocity distribution reduces Doppler broadening, which gives sharp spectral lines.

3.2.3 Pulsed Supersonic jet and vacuum set-up

Pulsed valves for the supersonic jet ensures high gas density at the orifice. They give higher transient beam densities yet require lower average carrier rare gas. This decreases the load on the pumping system. Thus, employing a pulsed nozzle significantly reduces consumption of expensive rare gas carriers.

Pulsed valve and nozzle

A slit nozzle is a pair of jaws mounted on a block. To achieve a uniform distribution of the expansion gas across the slit, the block is designed with six cylindrical channels with different diameters. This block is mounted on a pulsed solenoid valve (Parker Hannifin Corporation, General Valve Series 9), the opening and closing of valve is controlled by an Iota One valve driver. The alignment of slit jet nozzle in the six-way cross is shown in Figure 3.3. During

this experiment methanol at -75^{o}C was circulated around the slit nozzle using a cold copper jacket and the circulating methanol was cooled by a Neslab Endocal Refrigerator. Cooling of the nozzle was very crucial in observing benzene-noble gas trimers.

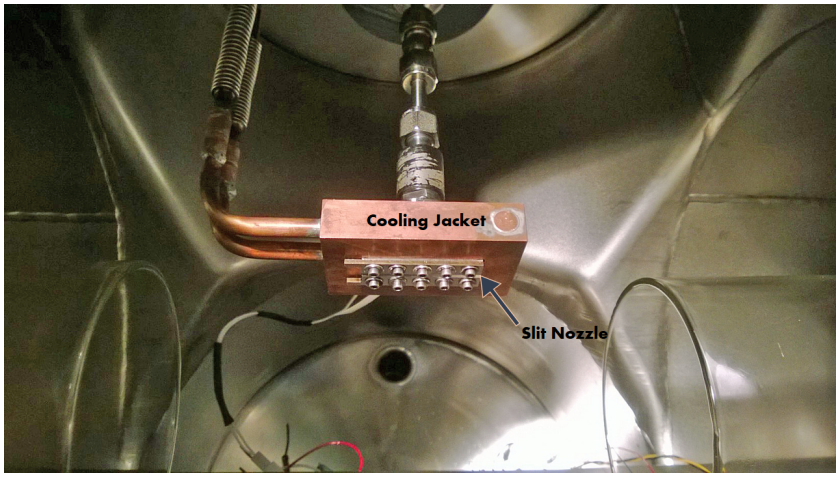

Figure 3.3: Pulsed slit nozzle and cold jacket configuration inside the vacuum chamber.

Six-way cross vacuum chamber

The pulsed slit jet nozzle and the multipass cell are all inside a six-way cross vacuum chamber (Figure 3.1). A 10" diffusion pump (Varian, VHS-10) backed by a mechanical pump (Edwards, EM275) is used to evacuate the six-way cross. During the operation of the supersonic jet the pressure inside the vacuum chamber is kept as low as 10^{-7} Torr.

3.3 Astigmatic Multi-pass Cell

The concentration of clusters in supersonic expansion is small ($\sim 10^{13}$ clusters/cm^3) and when detecting a weak absorption band like a combination or an overtone band the change in the laser intensity is small with respect to the initial laser intensity. So, the sensitivity is limited by the laser fluctuations. In order to increase the sensitivity, a long absorption pathlength is required, and since the expansion region is small this has to be done in a limited space. One of the best ways is to use an astigmatic multipass cell. In an astigmatic

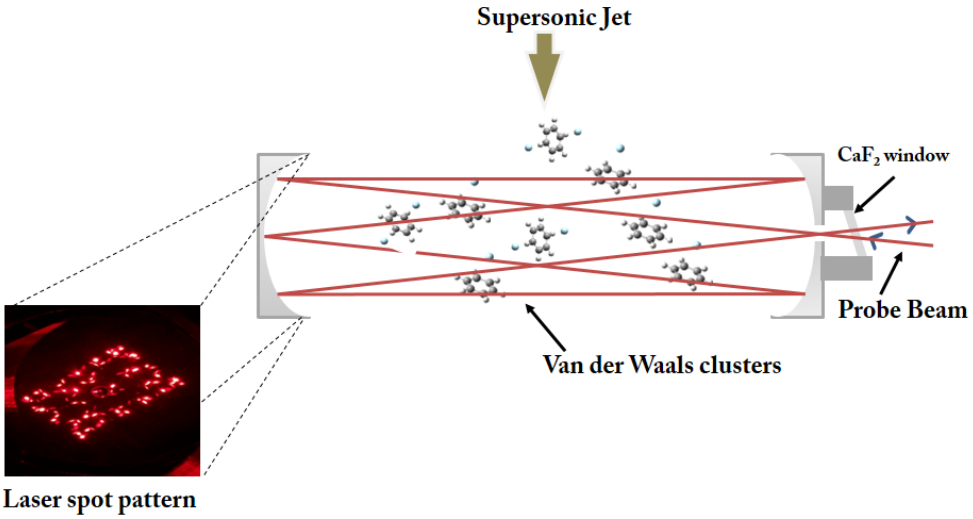

Figure 3.4: Schematic of the astigmatic multipass absorption cell with van der Waals cluster formation in the cell. The laser beam enters in an off-axis direction and exits at an angle from the input direction. The astigmatic mirror with the coupling hole with CaF_2 window at Brewster angle.

multipass cell long absorption path lengths can easily be achieved and interference fringes can be suppressed easily [43]. The multipass cell employs astigmatic or toroidal mirrors. A toroidal mirror has two different radii of curvature whose axes are orthogonal. The laser beam is injected through a hole in one mirror in an off-axis direction, the laser beam recirculates for a number of times and exits back through the coupling hole (Figure 3.4). The multipass cell used in our set-up (Aerodyne Research Inc., AMAC-100) is 70 cm long and can provide 182 passes.

3.4 Optical Parametric Oscillator probe for van der Waal cluster spectroscopy

Optical Parametric Oscillator (OPO) is a new generation of coherent light source which is gaining recognition in spectroscopy. OPO's are known for their wide frequency tunability, narrow linewidth and high power. This section will give a brief summary of the basic working principle and employing OPO in the set-up.

3.4.1 Working principles of Optical Parametric Oscillators

An Optical Parametric Oscillator is very similar to a laser with a resonator design, but unlike a laser, where the optical gain is from stimulated emission, in OPO the gain is obtained from a process called parametric amplification. Parametric amplification involves the conversion of a high intensity pump beam at frequency ω_{p} to a lower frequencies signal (ω_{s}) and idler (ω_{i}) in a nonlinear crystal with large second order non-linear susceptibility. This can be also pictured as the pump photon converting into two lower energy photons, signal and idler, satisfying the conservation of energy

$$\omega_{\mathrm{p}} = \omega_{\mathrm{s}} + \omega_{\mathrm{i}}, \tag{3.6}$$

and conservation of momentum,

$$\mathbf{k}_p = \mathbf{k}_s + \mathbf{k}_i. \tag{3.7}$$

where $\mathbf{k}$ is the wavevector. The conservation of momentum is the phase matching condition which determines the wavelength of the idler and the signal. When the phase matching condition is satisfied, amplitudes add up constructively from different parts of the crystal and thus high power conversion efficiency is ensured. The most effective phase matching technique used by OPO's is quasi phase matching. In a crystal with high non-linear susceptibility like $LiNbO_3$ this is done by flipping the electric polarization of the crystal at the effective interaction length of parametric generation or coherence length in a periodic fashion. This is achieved by the application of an electric field and the process is called periodic poling. The grating period determines the signal and idler wavelength.

The optical resonator or cavity in OPO provides feedback to the chosen frequency to the gain medium, high reflectivity mirrors are chosen for signal or idler frequency (singly resonant OPO) or for both signal and idler (doubly resonant OPO). The OPO system we are using (Lockheed Martin Argos Model 2400 - Module D) is a singly resonant OPO for the idler as shown in Figure 3.5. The idler frequency region in this OPO covers a frequency range from 3.9 to 4.6 μm (2173 to 2564 cm^{-1}). The signal wavelength is between 1.3 to 1.4

μm and pump wavelength is at 1.064 μm. The nonlinear crystal in the OPO is a magnesium-oxide doped periodically-poled lithium niobate (MgO:PPLN), with anti-reflection coating for signal, idler and pump wavelengths. MgO doping of PPLN increases the damage threshold. The grating on the periodically poled lithium niobate (PPLN) crystal is fanned out (Figure 3.6), the idler frequency tuning is achieved by translation of crystal across the pump beam. The translation changes the poling period that the pump beam is exposed to, which changes the phase matching condition and consequently the wavelength. Figure 3.5 shows the crystal using a single axis translational stage. The crystal is mounted in a temperature controlled oven and it needs to be temperature stabilized between 45°C and 70 °C with a precision of 0.1° C. Coarse tuning of the wavelength is possible by changing the temperature, since changing temperature changes the refractive index. The temperature stabilization of crystal is time consuming, hence, crystal position tuning is preferred.

The OPO pump laser source is a diode pumped fiber optic laser with a power output of 10 W at 1.064 μm. The seed laser for the 10 W fiber amplifier is a distributed feedback laser (DFB). The DFB laser source has a power of 10 mW and a linewidth of 100 KHz. The piezoelectric transducer (PZT) strain of the fiber provides fine tuning and scanning of the pump laser frequency. A 0-100 V signal applied to the PZT element from PZT driver allows a continuous idler frequency tuning over a 2 cm^{-1} range.

3.4.2 The experimental set-up with OPO source

Description of the set-up

Operation and data acquisition process

Each scan was acquired over a frequency window of 0.75-1 cm^{-1}. This frequency window was achieved by driving the PZT of the seed laser using a sine wave of 40 V amplitude and 100 Hz frequency. The sine wave was generated using a function generator. The data was taken only on the rising part of the sine wave and near the zero crossing, where it is most linear.

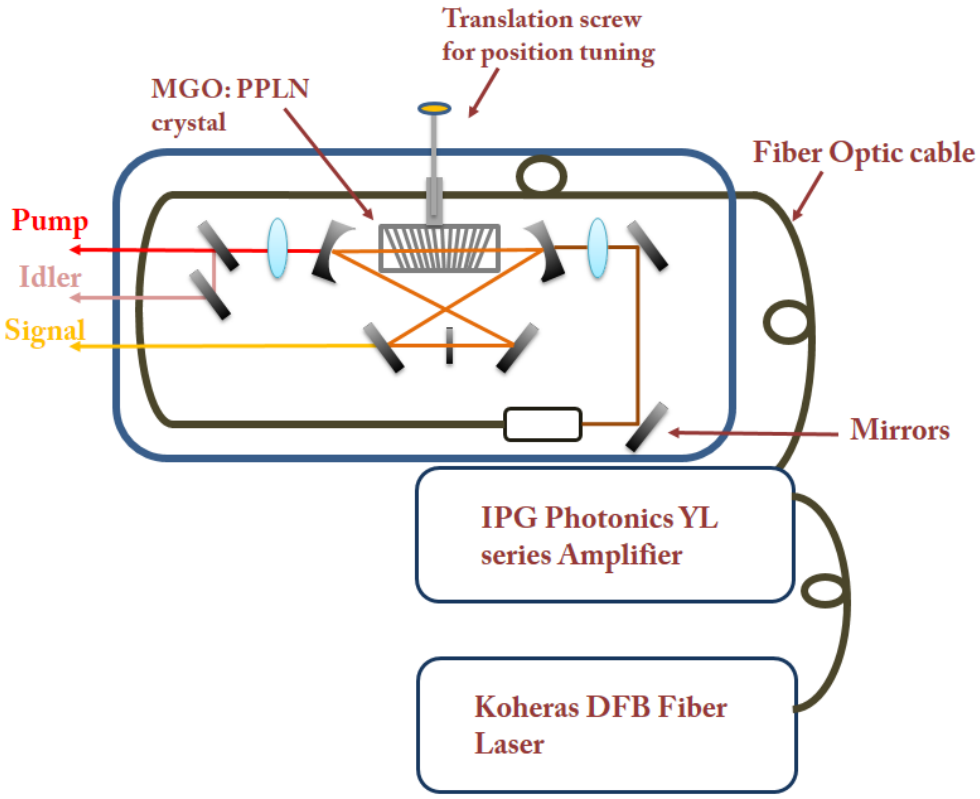

Figure 3.5: Schematic of the OPO module showing the MgO doped Periodically Poled Lithium Niobate crystal (MgO:PPLN) with fanned out grating, the DFB fiber laser and Fiber amplifier as the pump for the OPO.

So, synchronization and sequencing is crucial in the data acquisition. A TTL signal is used as a reference for this purpose, it was generated from the same waveform generator with the same frequency as the sine wave. The TTL signal was sent to a timer card, which triggers the counter-1, this counter acts as a reference for other counters. Counter 1 sends out a signal to activate the other counters (2, 3). As shown in the Figure 3.7, counter 2 initiates the data acquisition process and counters 3 is responsible for setting the time for opening of the valves. The Counter 2 value is set in such a way that the data is acquired along the linear part of the sine signal. The valves remain open for 4 ms. Once, the absorption signal is acquired it is subtracted from the background which is taken when the valve is closed. The

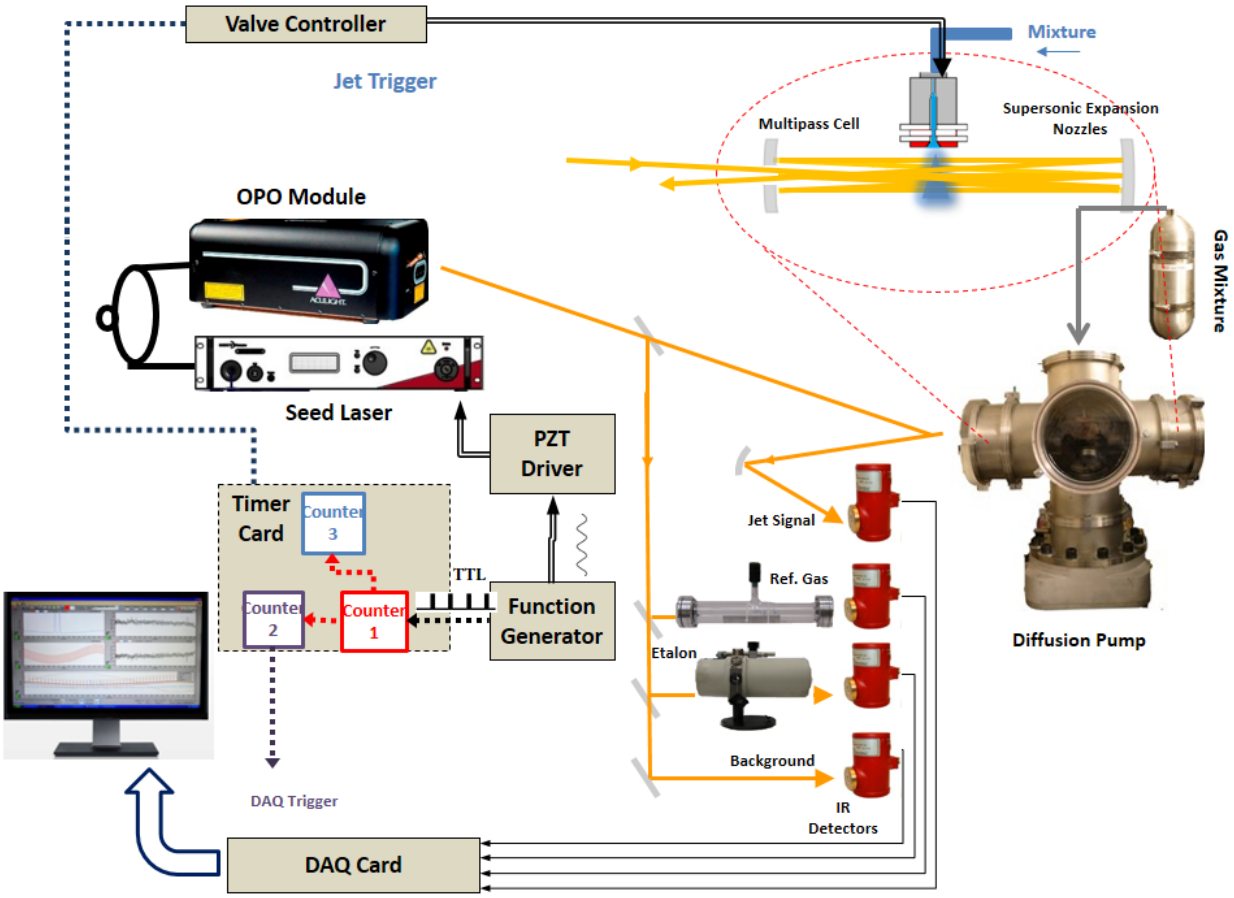

Figure 3.6: Illustration of the OPO experimental set-up. Laser beams are shown with solid yellow lines, data signals with black lines, and synchronizing signals with dotted lines.

repetition rate of the scans is largely dependent on the time required by the diffusion pump to exhaust the gas molecules from the six-way cross chamber, this may take 3 to 5 seconds. Depending on the desired signal-to-noise ratio, each scan is averaged over 100 to 500 gas pulses. The spectrum of a reference gas (N_2O or CO_2) and etalon is acquired simultaneously to calibrate the absorption spectrum of the van der Waals clusters in wavenumber scale. The reference gas is kept in a glass cell with calcium fluoride window. The calcium fluoride has a wavelength transmission of more than 90% from 0.1 to 8 μm.

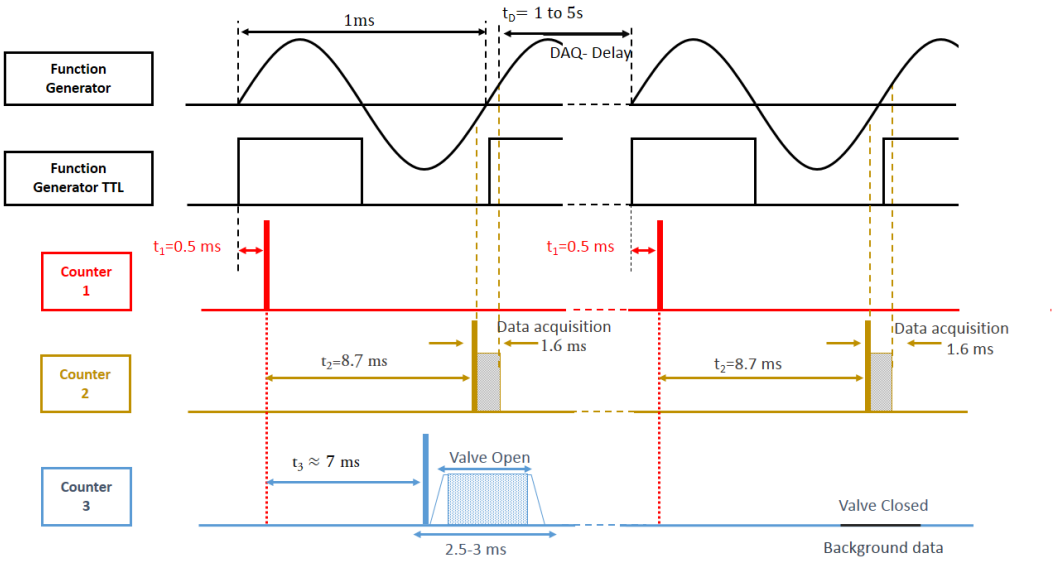

Figure 3.7: Schematic diagram illustrating the timing sequence for data acquisition in OPO set-up [12]. The red dotted lines shows the counter 2 and 3 are triggered by counter 1

Data acquisition software

All the data acquisition is managed by a LabVIEW program. A computer screen-shot of the program is shown in Figure 3.8. This program controls the timers and the DAQ card. The program collects data from four channels, the jet, reference, etalon and a fourth channel, which will be discussed in the next section. The program subtracts the jet signal from the laser background. To suppress the very high frequency noise in the jet spectrum, a digital filter is used. The generated data are single-column text files which have intensities for 16000 bins. These files are processed and calibrated using the Thermo Scientific $GRAMS/AI^{TM}$ software.

3.4.3 OPO frequency stabilization

Frequency stabilized sources are required for high resolution rovibrational spectroscopic measurements. Usually, the frequency of the laser sources tends to jitter due to mechanical vibrations, temperature instabilities, air pressure changes, and laser current noise. Due to

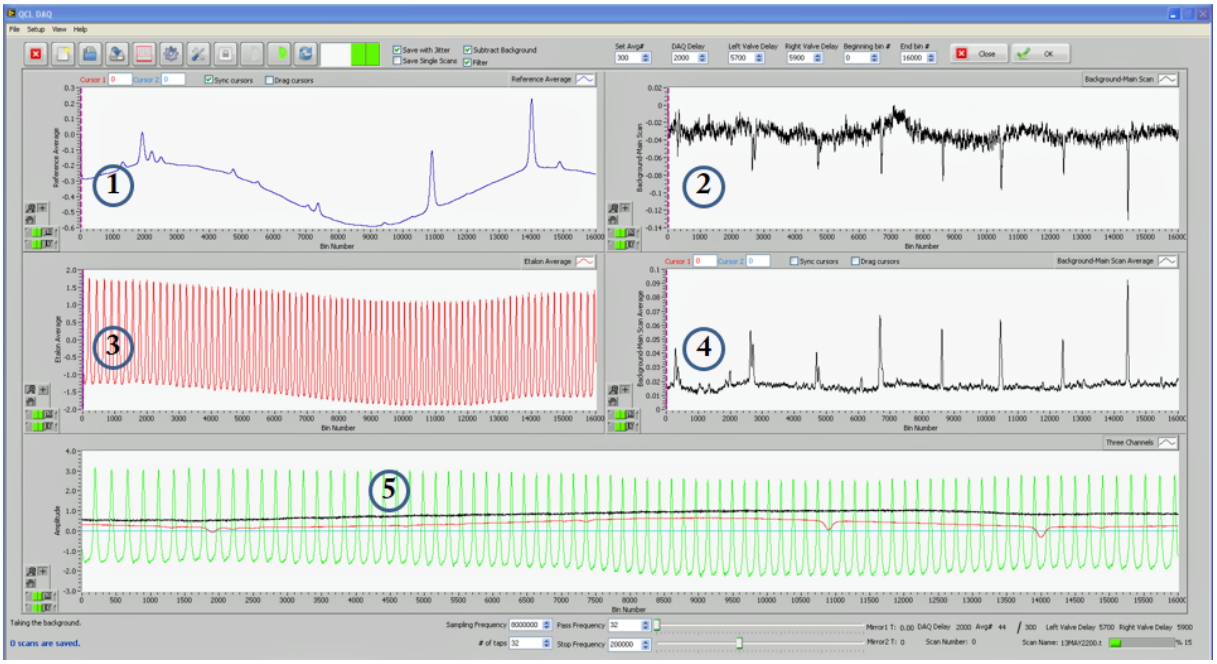

Figure 3.8: Screen-shot of the LabVIEW data acquisition program, four channels are shown in the figure. (1) Channel which gives the average reference gas spectrum (2) average supersonic jet spectrum (3) average etalon signal (4) Channel 4 gives the jet signal after substraction with the background signal, which cancels the power fluctuations and high frequency (5) single current scans of all three channels.

these fast jitters of the laser frequency, one can observe significant line broadening while averaging the signals. Consequently, this decreases the resolution of the spectra and degrades the signal to noise ratio.

In order to suppress these short-term frequency jitters, we used a digital signal processing technique. This technique makes use of the fact that the laser frequency shift due to the jitter is random in nature. We chose the first scan as the reference scan, based on which the program calculates the shift of the current scan with respect to the reference. This shift is an average shift calculated based on etalon peaks due to the nonuniformity of the jitter. LabVIEW advanced Peak Detector VI was used for the accurate detection of peaks. Each scan is shifted by adding or subtracting the shift to the scan to match the frequency with the reference scan and the scan is averaged subsequently. Figure 3.9 shows a front panel

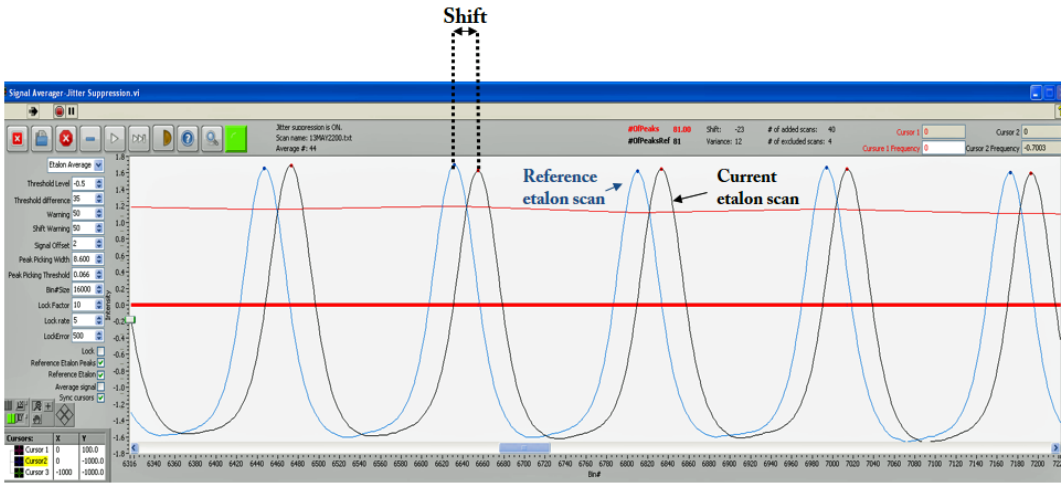

Figure 3.9: A screen-shot of the jitter suppression window, showing a portion of the reference etalon signal as blue trace and the current etalon signal as the black trace. The shift of etalon peaks in each scan is calculated by the jitter suppression program relative to the peaks of the reference signal peaks.

scree-shot of jitter suppression program.

3.4.4 SRO-OPO Power fluctuation suppression and background subtraction

For random noise reduction signal averaging is quite effective, since averaging increases the signal strength by averaging out the noise. In the case of OPO, there are also fluctuations in the spectra which are due to power fluctuations of the pump laser [39]. These fluctuations are not random in nature, instead they add-up with signal averaging and obscures the weak absorption lines. A previous study by W. Chen et al. [38] used a balanced detection technique, where the power fluctuation is removed by electronically subtracting the idler beam from the signal beam. We implemented a similar set-up, where a reference beam separated from the probe laser source is used instead of the idler beam. The power fluctuation is then removed by electronically subtracting the reference beam from the absorption signal [12]. There is an extra channel for collecting the background signal was employed as shown in Figure 3.6. The subtraction was done by using the LabVIEW program. Figure 3.10 shows

the screenshot demonstrating the implementation of the suppression of power fluctuations in OPO.

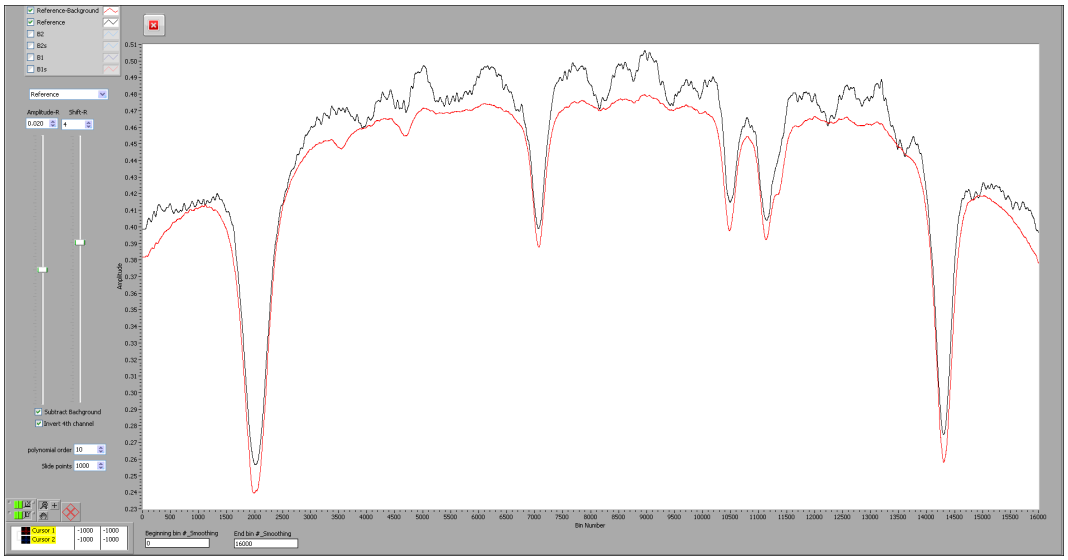

Figure 3.10: The screen-shot of the computer screen, showing the effect of background subtraction on suppressing the power fluctuation. The black trace is before and the red trace is after implementing the suppression technique.

Chapter 4

Infrared spectra of $C_6D_6 - Rg_n (n = 1, 2)$

4.1 Introduction

Weakly-bound rare gas (Rg) − benzene clusters provide attractive model systems for progressive solvation of an organic molecule, and their spectroscopy with rotational resolution has an extensive history [11]. Thus, for example, electronic spectra have been obtained using laser induced fluorescence, coherent ion dip, or resonant enhanced two photon ionization techniques for the complexes containing benzene together with He [14, 17], Ne [19], Ar [21] - [23], Kr [24], and Xe [24], nonlinear Raman spectroscopy to He [25] and Ar [26], and microwave spectroscopy to Ne [27, 28], Ar [26, 29], Kr [30], and Xe [26]. Rg − benzene dimers and trimers are found to have a simple structure in which the rare gas atom is on the average located on the C_6 symmetry axis at a distance of about $r_0 = 3.4 - 3.8$ Å (depending on the species) above and/or below the plane of the benzene molecule. The point group symmetry of dimer reduces to C_{6v} from D_{6h} for the benzene monomer, and the point group of the trimer remains the same as the monomer.

However, there have been no previous studies of Rg − benzene complexes in the infrared region. This thesis reports such a study. This chapter discusses the analysis of the infrared spectra of $C_6D_6 - Rg_n$, (n=1,2) in the region of the ν_{12} C−D stretching band of C_6D_6 near 2289 cm^{-1}, where the rare gas (Rg) being He, Ne, or Ar. There have been very few previous spectroscopic observations of $He_{1,2}$− benzene. This work also represents the first observation in any spectral region of the $He_{1,2}$− and $Ne_{1,2}$− C_6D_6 isotopologues.

C_6D_6 is chosen instead of C_6H_6 because C_6H_6 has no fundamental vibrations in our laser region. The molecular structure of C_6D_6 and C_6H_6 are the same, so the structures and intermolecular distance are similar. There is a strong Fermi (anharmonic) resonance between

the fundamental band ν_{12} ($\approx$2289 cm^{-1}) and the combination band $\nu_2 + \nu_{13}$ ($\approx$2276 cm^{-1}). So, we actually observed two bands for the dimers and the trimers. The ν_{12} fundamental band of C_6D_6 monomer was analyzed in detail by Plíva, et al. [31] in 1994. Here we report the molecular parameters by fitting a simple symmetric rotor to the fundamental and combination bands of the dimers and the trimers.

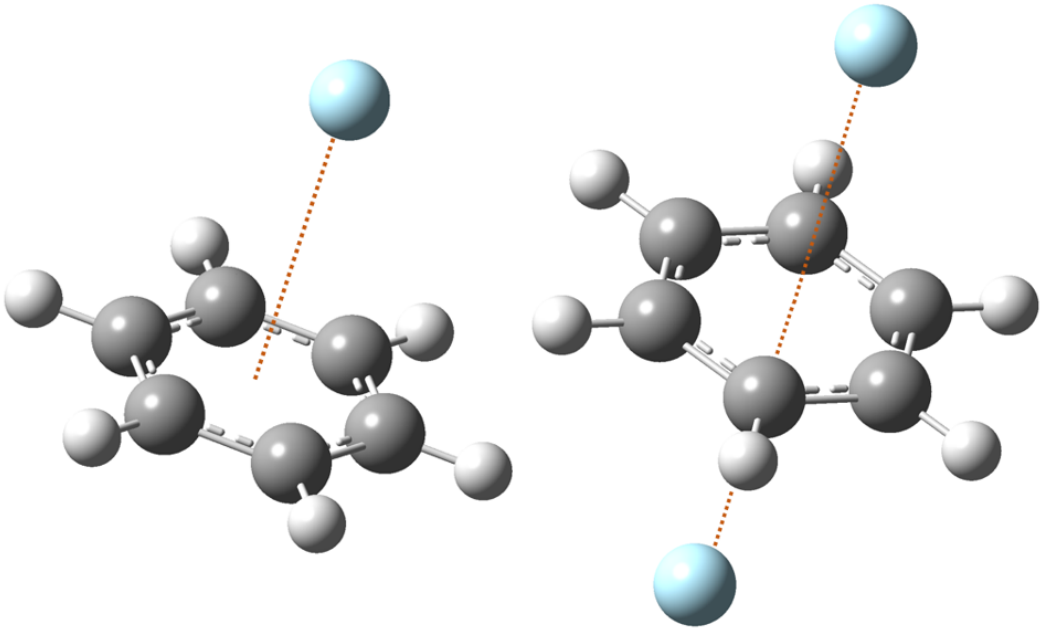

Figure 4.1: Structure of the dimer $C_6D_6 - Rg$ on the left and the trimer $C_6D_6 - Rg_2$. The red trace shows the intermolecular distance between the rare gas and center of mass of the benzene.

4.2 Results

Experimental Conditions

Spectra were recorded using the experimental set-up described in Chapter 3. For all the gas mixtures the laser was scanned from about 2274 cm^{-1} to 2291 cm^{-1}. CO_2 gas was used as reference gas for frequency calibration of the complex spectra. The expansion gas mixtures contained approximately 0.1% C_6D_6. Higher concentration of C_6D_6 resulted in freezing of

the nozzle. The carrier gas was He for $C_6D_6 - He_{1,2}$, a 1:2 mixture of Ne:He for $C_6D_6 - Ne_{1,2}$, and a 1:5 mixture of Ar:He for $C_6D_6 - Ar_{1,2}$. The ratios of the gas mixture was optimized to obtain the maximum concentration of complexes in the jet. The backing pressure of the gas sample in the reservoir were about 9 atm, this was increased to 13 atm for the observation of trimer.

Simulation and fitting of data

The objective is to determine the molecular parameters for the ground and excited state mentioned in the rotational energy as given by Equation 2.51. The PGOPHER computer program [35] was used for spectral simulation which is a general purpose program for simulating and fitting rotational, vibrational and electronic spectra with a graphical user interface. In order to begin with the simulation, the easiest way is to guess the structure of the vdW complex. I considered the symmetric top structures for the dimers and trimers as shown in Figure 4.1 These structures were considered from some of previously determined structures using microwave and electronic spectra [11].

The rotational constants of the assumed structure were derived using a program that determines the principal moments of inertia of the molecules (PMIFST) [44]. These rotational constants were used to create a simulation for an initial comparison with the observed spectra. Some of the parameters need to be fixed before assigning the transitions frequencies: the rotational temperature, the line shape, point group symmetry of the complex, nuclear statistical weights (Section 2.6.1) and the symmetry element of the ground and excited vibrational state.

As discussed in Section 2.4, the rotational constant of a symmetric top around the symmetry axis (A or C) cannot be easily determined from parallel bands. The position of rare gas atoms for the dimers and the trimers, as shown in Figure 4.1, does not change the moment of inertia about the C_6 symmetry axis. Hence, the parameter A or C for the ground vibrational state of $C_6D_6 - Rg_{1,2}$ complexes were fixed at the C_6D_6 monomer C value, 0.078496 cm^{-1},

determined previously by Plíva et al. [30, 36]. It should be noted that C_6D_6-$He_{1,2}$ complexes are oblate symmetric tops, C_6D_6-$Ne_{1,2}$ and C_6D_6-$Ar_{1,2}$ are prolate symmetric tops (Section 2.3.1).

For a symmetric top, the spectral pattern follow the selection rules for parallel or perpendicular band, as described in Section 2.6 (Equations 2.69 and 2.70). Since, the observed band is C-D stretch (ν_{12}) and ring stretch ($\nu_2 + \nu_{13}$) vibrational mode, the change in dipole moment is perpendicular to the symmetric top axis of the benzene. Hence, the observed band is perpendicular. Each observed line is a transition between the rotational quantum numbers J and K, with the selection rules one can determine the allowed transitions. Lower K lines are assigned first, the low J lines are usually located near the band center. Each J value, the corresponding K lines are assigned by varying a minimum number of parameters. Eventually, 15 parameters were varied and determined from the simulation for the dimers. The ground state molecular parameters were rotational constant B'' and centrifugal distortion constants D_{JK}'' and D_J''. The excited state parameters determined for the fundamental and combination band are vibrational band origins ν_0, rotational constants B', C' or A', the centrifugal distortion constants D'_{JK}, D'_J and the coriolis coupling constant ζ'. Similarly, 11 parameters were determined for trimers. Distortion constants were not determined for trimers due to fewer number of observed lines and the fact that these are heavier species.

The spectra were fitted to symmetric top structures as shown in the Figure 4.1. The assumed Gaussian line width was 0.002 cm^{-1} (60 MHz). The simulated spectra used an effective rotational temperature of 2.5 K for the dimers and 1.5 K for the trimers. Nuclear spin weights for the point group symmetry of C_{6v} and D_{6h} are given in Table 4.1.

4.2.1 $He_{1,2} - C_6D_6$

Three previous publications on the $C_6D_6 - He_{1,2}$ complex are especially relevant here. The first, from 1979, is a pioneering laser induced fluorescence study of the electronic spectrum by Beck et al. [14], who studied the $S_1 \leftarrow S_0$ 6_0^1 ($\nu_6 1 \leftarrow 0$) vibronic band ($\approx$38610 cm^{-1}) in

a pulsed supersonic jet expansion with an effective rotational temperature of about 0.3 K. The spectrum was remarkably clear and clean, but the accuracy of their fitted parameters was limited by their spectral resolution ($\approx$0.04 cm^{-1}). Recently, the same spectrum was re-examined by Hayashi and Ohshima [17] under similar conditions, but with greatly improved resolution ($<$0.01 cm^{-1}) using resonant enhanced two photon ionization spectroscopy. Their analysis yields a value of $r_0 \approx 3.60$ Å for the effective distance between the He atom and the benzene plane for the dimer and trimer. The third key paper, by Lee et al. [25], describes nonlinear Raman spectroscopy results, together with an analytical potential energy surface for He$-$C$_6$H$_6$ which is based on high-level *ab initio* calculations. This potential surface yields a very similar value for r_0 (3.61 Å), and also gives a value of $r_e = 3.16$ Å for the equilibrium intermolecular separation, that is, the global minimum of the surface itself, at an energy of -89.6 cm^{-1}.

We observed C$_6$D$_6-$He and C$_6$D$_6-$He$_2$ spectra accompanying both the ν_{12} and $\nu_2 + \nu_{13}$ bands, as illustrated in Figure 4.2. The stronger lines were assigned to the C$_6$D$_6$ monomer, as described in Ref. [31], these strong C$_6$D$_6$ lines were removed from the Figure 4.2 for an effective comparison between the observed and simulated spectra of C$_6$D$_6-$He and C$_6$D$_6-$He$_2$. The dimer bands are roughly 6 times weaker than the monomer bands and trimer bands are 12 times weaker. The ground state rotational constant C is fixed as the monomer for all the complexes. We assigned and fitted 90 spectral lines in terms of 140 transitions for dimer and 60 spectral lines were assigned for 69 transitions for trimer, and varying a total of 16 parameters. This was a simultaneous fit, so that both observed band, fundamental and combination band helped to determine the ground state parameters.

The resulting molecular parameters for the C$_6$D$_6-$He dimer are given in Table 4.2. Note that it was possible to determine a value for the l-type doubling parameter q (see Section 2.5) for the $\nu_2 + \nu_{13}$ upper state (2275.96 cm^{-1} band) for C$_6$D$_6-$He, but not for the ν_{12} fundamental (nor for any of the He$_2-$, Ne$_{1,2}-$ or Ar$_{1,2}-$ C$_6$D$_6$ bands below). The simulated

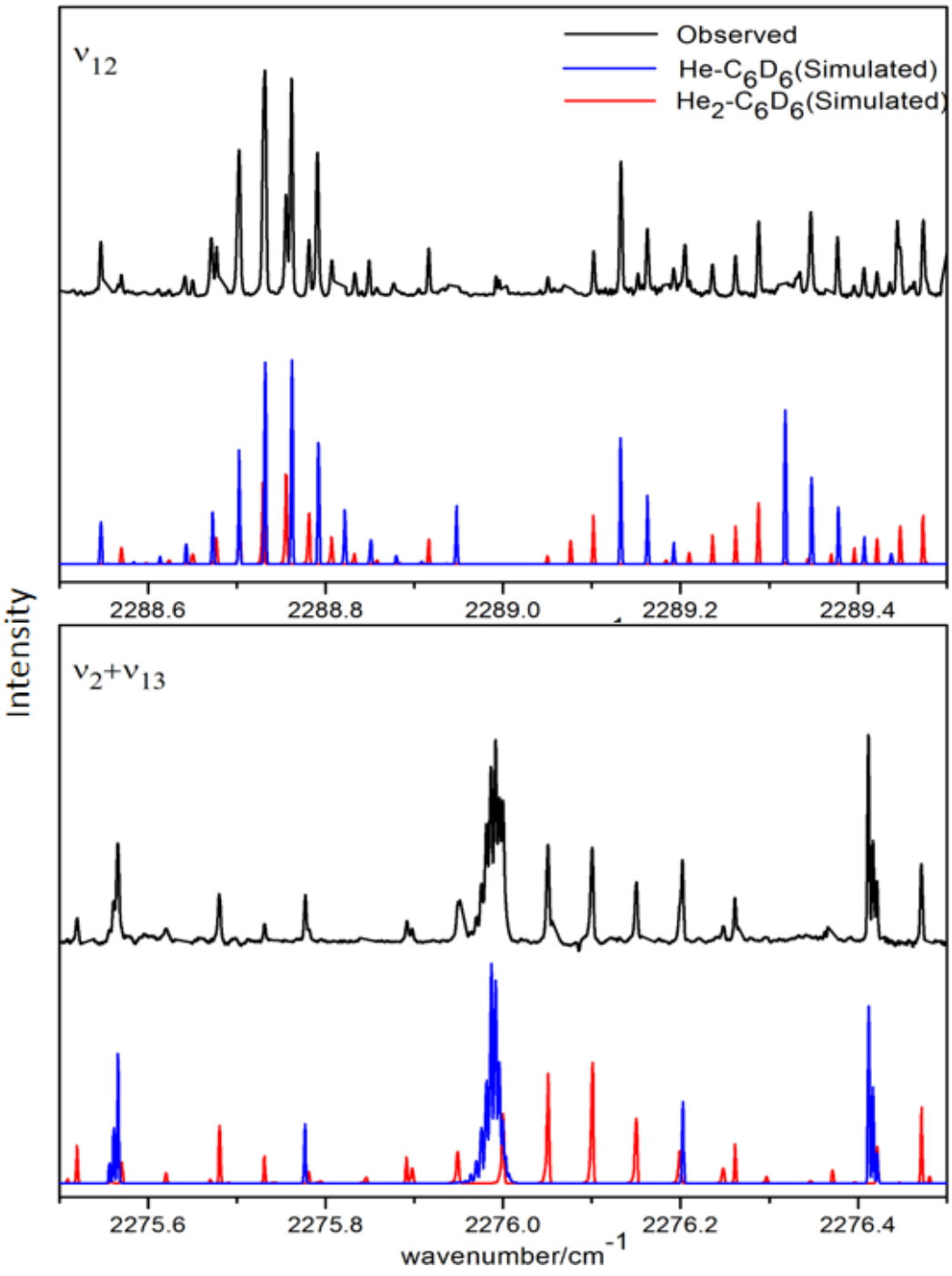

Figure 4.2: Observed (black trace) fundamental ν_{12} band (top) and $\nu_2+\nu_{13}$ bands (bottom). The simulated (blue and red trace) spectra of C_6D_6-He dimer is shown in blue trace and $C_6D_6-He_2$ trimer in red trace.

spectra are based on these parameters and assume a temperature of 2.5 K for the dimers and 1.5 K for the trimers with line widths of 0.0029 cm^{-1} and 0.002 cm^{-1}, respectively (Figure 4.2). They are calculated using the parameters from Table 4.2. For simulating the intensity, we also included nuclear spin statistical weights of rovibrational levels (Section 2.6.1), which are given in Table 4.1.

Table 4.1: Nuclear spin weights of respective symmetries for C_{6v} (dimer) and D_{6h} (trimer)

C_{6v}	A_1, A_2	B_1, B_2	E_1	E_2
	130	119	232	248

D_{6h}	A_{1g}, A_{1u}	A_{2g}, A_{2u}	B_{1g}, B_{1u}	B_{2g}, B_{2u}	E_{1g}, E_{1u}	E_{2g}, E_{2u}
	74	56	55	64	116	124

The molecular parameters for C_6D_6−He_2 are given in Table 4.3. The centrifugal distortion constants (see Section 2.4) for the trimers were not determined because of fewer number of assigned lines.

4.2.2 $Ne_{1,2} - C_6D_6$

The C_6H_6−Ne dimer has been studied by electronic [17] and microwave [26,27] spectroscopy, but there are no previous reports of dimer C_6D_6−Ne or trimer C_6D_6−Ne_2 in the IR region. The dimer and trimer spectra are shown in Figure 4.3. A total of 63 lines were fitted in terms of 199 transitions in a simultaneous analysis to give the C_6D_6−Ne parameters listed in Table 4.2. For trimer C_6D_6−Ne_2, 46 lines were assigned in terms of 67 transitions given in Table 4.3. The ground state constant for rotation around the symmetric top axis (this is now labelled A) was again fixed at the monomer C-value. We noted that the microwave values of the distortion constants D_{JK} and D_J are quite similar for C_6H_6−Ar and C_6D_6−Ar [28], therefore estimated values of these constants for C_6D_6−Ne by simple scaling of those of C_6H_6−Ne [26] according to their ratios for the Ar complexes. These scaled values were held

fixed in the analysis for the ground and excited states. Considering these constraints, there were 9 adjustable parameters in the fit (see Table 4.2).

4.2.3 $Ar_{1,2} - C_6D_6$

Benzene - Ar dimers have been extensively studied in the past; see Fernández et al. [37] for a recent high level *ab initio* calculation and references to other work. In particular, the microwave spectrum of C_6D_6−Ar was reported by Brupbacher and Bauder [28]. Thus accurate ground state constants (B, D_{JK}, D_J) were already available for this species, making our assignment of the spectra shown in Figure 4.4 relatively easy. Since our expansion gas was 80% helium, some C_6D_6−He transitions were also weakly visible. The strong C_6D_6 monomer lines and C_6D_6−He are removed. A total of 89 lines involving 307 transitions were fitted to give the C_6D_6−Ar parameters listed in Table 4.2 and 97 spectral lines were fitted for 126 transitions to give the C_6D_6−Ar_2 parameters listed in Table 4.3. With the ground state parameters all fixed, a total of 12 excited state parameters were adjusted, including D_{JK} and D_J for both upper states.

4.3 Discussion and conclusions

Evaluating the results in Table 4.2, we note that the Coriolis interaction parameter, ζ, tends to increase slightly in magnitude when rare gas atom is added to C_6D_6. As might be expected, the increase is larger for Ne than for He, but then it tends to fall back a bit for Ar. This is quite similar to the trend observed for ζ in the upper state of the $S_1 \leftarrow S_0$ 6_0^1 vibronic bands of C_6H_6−Rg complexes [17, 19]. For trimer complex with one more rare gas atom the Coriolis coupling parameter from Table 4.3 decreases with respect to the corresponding dimer complex. We also note that the changes in rotational constants upon vibrational excitation to the ν_{12} and $\nu_2 + \nu_{13}$ states for the Rg complexes are small, and tend to be similar to those of C_6D_6 itself.

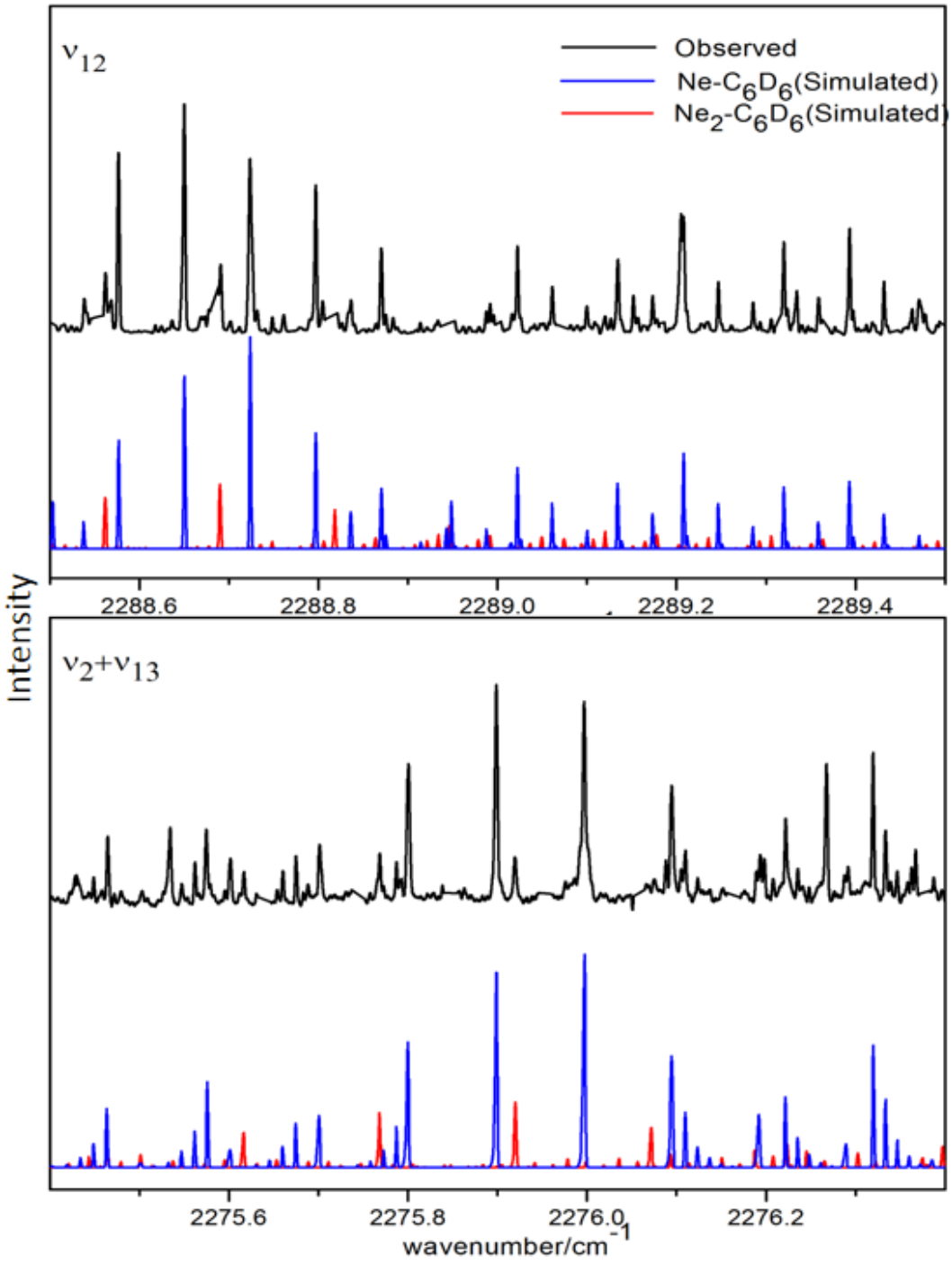

Figure 4.3: Observed (black trace) fundamental ν_{12} band (top) and $\nu_2+\nu_{13}$ bands (bottom). The simulated (blue and red trace) spectra of C_6D_6-Ne dimer is shown in blue trace and $C_6D_6-Ne_2$ trimer in red trace.

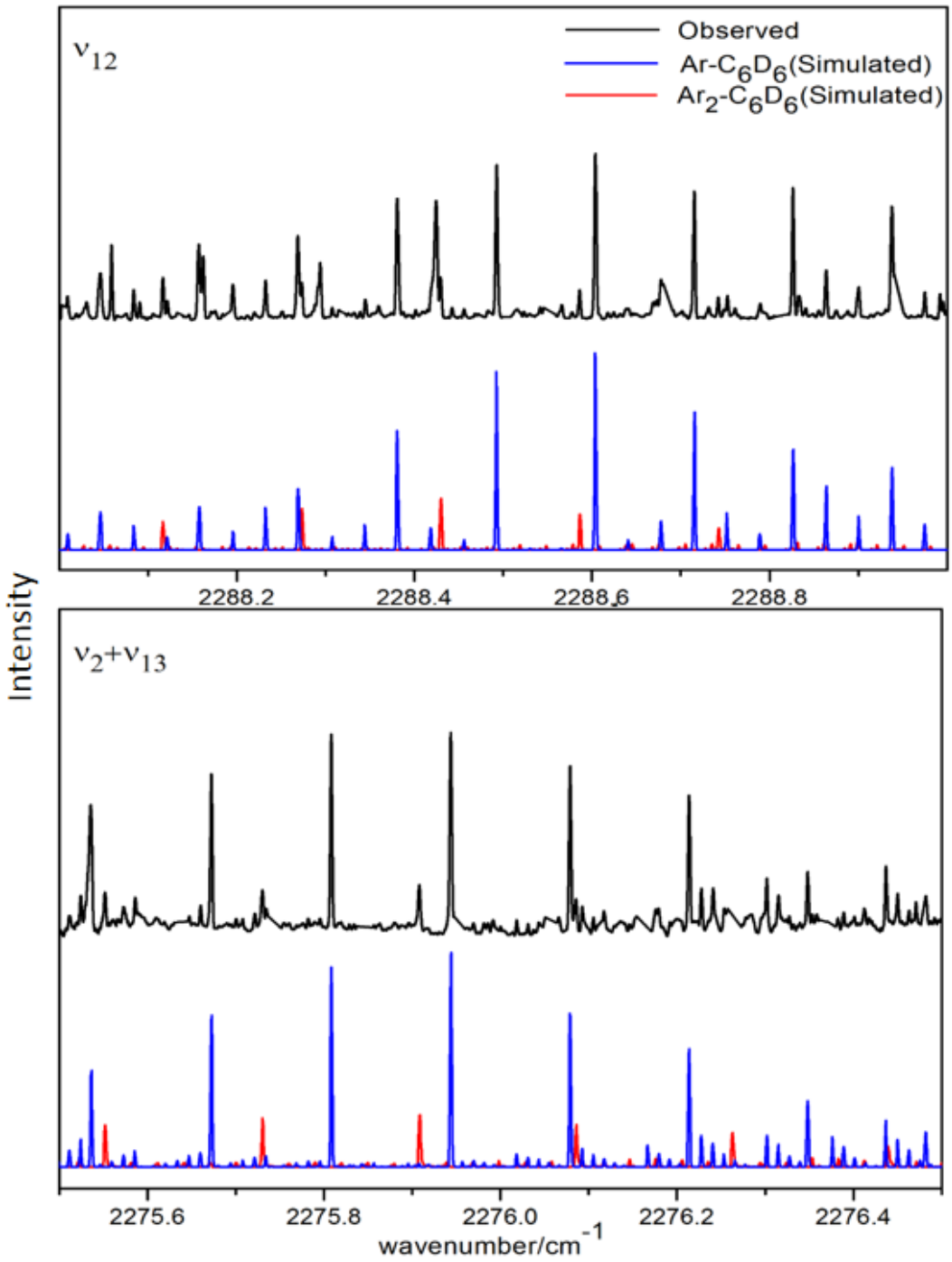

Figure 4.4: Observed (black trace) fundamental ν_{12} band (top) and $\nu_2+\nu_{13}$ bands (bottom). The simulated (blue and red trace) spectra of C_6D_6-Ar dimer is shown in blue trace and $C_6D_6-Ar_2$ trimer in red trace.

Table 4.2: Molecular parameters for the C_6D_6[a] and C_6D_6 − Rg complex (in cm^{-1}). Uncertainties in parenthesis are 1σ from the least-squares fits in units of the last quoted digit.

	C_6D_6 [31,36][b]	C_6D_6 − He	C_6D_6 − Ne	C_6D_6 − Ar
Ground state				
B''	0.15701902	0.107559(23)	0.056149(17)	0.03710704
$C''(A'')$[c]	0.078496	0.078496	0.078496	0.078496
$D_{JK}''\times10^{-7}$	-0.4174	14.7(69)	24[d]	4.847
$D_J''\times10^{-7}$	0.25	0.01(51)	5.3[d]	0.892
Excited state combination band				
ν_0	2275.8776(1)	2275.9621(2)[e]	2275.9206(2)	2275.8498(1)
B'	0.1567464(68)	0.107577(22)	0.056147(17)	0.0370964(28)
C'/A'	0.0783580(50)	0.078350(18)	0.078386(18)	0.0783220(78)
ζ'	-0.33501	-0.34140(39)	-0.34482(36)	-0.33816(11)
$D_{JK}'\times10^{-7}$	-0.4174	-28.3(55)	24	5.45(86)
$D_J'\times10^{-7}$	0.25	37.7(44)	5.3	0.33(20)
Excited state fundamental band				
ν_0	2288.7395(2)	2288.7326(2)	2288.6725(2)	2288.5337(1)
B'	0.1568001(48)	0.107632(31)	0.056143(17)	0.0371050(23)
C'/A'	0.0784018(37)	0.078401(26)	0.078395(16)	0.0784608(76)
ζ'	-0.17017	-0.18180(33)	-0.18621(29)	-0.18347(10)
$D_{JK}'\times10^{-7}$	-0.4174	-47.9(91)	24	4.25(65)
$D_J'\times10^{-7}$	0.25	49.8(76)	5.3	0.5(15)

[a] Units of cm^{-1}, except for ζ which is dimensionless. Uncertainties in parentheses are 1σ expressed in units of the last quoted digit; parameters without uncertainties were fixed.
[b] $D_K = 1.88\times10^{-8}$ cm^{-1} for all C_6D_6 states.
[c] Parameter for rotation about the C_6 symmetry axis, assumed in the ground state to be equal to that of C_6D_6. This is labelled C for C_6D_6 and C_6D_6−He, or A for C_6D_6 −Ne and −Ar.
[d] Scaled from known [27] C_6H_6−Ne parameters by the ratio for C_6D_6−Ar and C_6H_6−Ar.
[e] Also: q = $-9.2(20)\times10^{-5}$ (l-type doubling parameter) for the 2275.9621 cm^{-1} state of C_6D_6−He.

A key result from the deuterated benzene − $Rg_{1,2}$ spectrum is the B-value, which directly gives the intermolecular separation with the assumption that the monomer structure remains unchanged in the dimer and trimer. A structure fitting program (STRFIT) [44] was used to calculate the intermolecular separation. This is obtained by assuming the monomer (benzene) structure and varying the distance between the benzene plane and the rare gas atom for the corresponding B-value. Experimental results for the intermolecular distances between He, Ne, or Ar and C_6H_6 or C_6D_6 for the dimer and trimer are summarized in Table 4.4. Table 4.4 thus confirms that our new B-values for C_6D_6 − $Rg_{1,2}$ are entirely consistent

Table 4.3: Molecular parameters for the C_6D_6 and C_6D_6−Rg_2 complex (in cm^{-1}). Uncertainties in parenthesis are 1σ from the least-squares fits in units of the last quoted digit.

	C_6D_6	$C_6D_6 - He_2$	$C_6D_6 - Ne_2$	$C_6D_6 - Ar_2$
Ground state				
B''	0.15701902	0.08014(25)	0.02888(3)	0.014855(16)
C''/A''	0.078496	0.078496	0.078496	0.078496
Excited state combination band				
ν_0	2275.8776(1)	2276.049(16)	2275.819(18)	2275.794(17)
B'	0.1567464(68)	0.08010(25)	0.02887(37)	0.01483(1)
C'/A'	0.0783580(50)	0.07833(4)	0.07710(2)	0.07830(2)
ζ'	-0.33501	-0.340(45)	-0.338(48)	-0.326(3)
Excited state fundamental band				
ν_0	2288.7395(2)	2288.728(1)	2288.611(18)	2288.336(1)
B'	0.1568001(48)	0.08008(23)	0.02886(3)	0.01494(1)
C'/A'	0.0784018(37)	0.07842(14)	0.07847(2)	0.07930(18)
ζ'	-0.17017	-0.186(4)	-0.185(4)	-0.175(38)

Table 4.4: Effective intermolecular distances for $Rg_{1,2}$-benzene in Å

	C_6H_6		C_6D_6	
	Rg	Rg_2	Rg	Rg_2
He	3.602(3)[a]	3.596(6)[a]	3.593(1)[b]	3.601(1)[b]
Ne	3.462[c]	–	3.455(1)[b]	3.438(17)[b]
Ar	3.586[c,d]	3.579[c,d]	3.580[c]	3.587(17)[b]

[a] Ref. [17].
[b] Present work.
[c] Ref. [27].
[d] Ref. [29].

with previous results [17, 27] for C_6H_6 − $Rg_{1,2}$. The intermolecular separation for He is the largest due to large zero point energy. Table 4.4 also shows the evident trend that the intermolecular distances increases as the rare gas atom becomes progressively more massive and more polarizable [17].

Vibrational shifts of the C_6D_6 − $Rg_{1,2}$ band origins relative to the C_6D_6 monomer are summarized in Table 4.5. These shifts are fairly small, the highest shift was observed for the ν_{12} band of C_6D_6−Ar and C_6D_6−Ar_2. In terms of direction, the shifts tend to be negative (red shifted) for the fundamental band and positive (blue shifted) for He and Ne for the combination band. A noticeable trend is that the frequency shift tend to increase with the

Table 4.5: Vibrational shift relative to C_6D_6 vibration in cm^{-1}

	shift ν_{12}	shift $\nu_2 + \nu_{13}$	ν_{12} minus $\nu_2 + \nu_{13}$
C_6D_6	0.0	0.0	12.862
$C_6D_6 - He$	-0.0069	$+0.0845$	12.771
$C_6D_6 - Ne$	-0.0668	$+0.0430$	12.752
$C_6D_6 - Ar$	-0.2058	-0.0278	12.684
$C_6D_6 - He_2$	-0.012	$+0.084$	12.68
$C_6D_6 - Ne_2$	-0.206	-0.028	12.79
$C_6D_6 - Ar_2$	-0.404	-0.084	12.54

addition of rare gas atoms. The last column of Table 4.5 shows that there is a small decrease in the separation between the ν_{12} and $\nu_2 + \nu_{13}$ band origins in going from the C_6D_6 monomer to the dimer and trimer. This could be indicating that, as the rare gas mass increases, there is a decrease in the magnitude of the Fermi interaction coupling these vibrations. On the other hand, it could be interpreted as simply being due to differing vibrational shift effects for the two vibrational modes.

Chapter 5

Conclusions

Rare gas - benzene van der Waals molecules were among the first weakly bound complexes investigated by laser spectroscopy in a supersonic jet. Since 1979 [14], the interest in such species has continued to the present time, the main reason being the simplicity of the intermolecular forces among these species. Thus, the quantitative comparison between the experiment and *ab initio* calculation of clusters is considered feasible. The infrared study of complexes leads to detailed information regarding the vibrationally averaged structure. The formation of structure is governed by the intermolecular forces. Information pertaining to these intermolecular interactions is contained in the experimental results.

The experimental results were obtained using the set-up described in chapter 3. The thesis discussed the improvement implemented on the experimental set-up. The implementation of OPO as the probe laser and increasing of the signal to noise ratio by suppressing the power fluctuations of the OPO laser. Also, the cooling of the supersonic-jet nozzle by circulating with methanol at -75^{o}C was implemented for the present work, which enabled the observation of the benzene - rare gas trimer complexes that is discussed.

This thesis presents an investigation on deuterated benzene - rare gas (Rg) dimer and trimer complexes using high resolution infrared spectroscopy. The rare gas used were He, Ne and Ar. The thesis reports the first study and observation of benzene $-$ $Rg_{1,2}$ complexes in the infrared region and also reports the first observation of $C_6D_6 - Ne_2$ in any spectral region. A strong Fermi resonance between the fundamental band ν_{12} and the combination band $\nu_2 + \nu_{13}$ were observed for each dimer and trimer. The present work on $C_6D_6 - Rg_{1,2}$ complexes were observed with an effective rotational temperature of about 2.5 K for the dimers and 1.5 for the trimers. The spectra were observed with a resolution of $\sim$ 60 MHz

which is the highest observed for benzene - rare gas complexes. The results presented for the dimers were published in Chemical Physics Letters [46].

The rotational parameters were determined by simulating the observed spectra. The structure of the complexes and the intermolecular distances were derived from the rotational parameters. The $C_6D_6 - Rg_{1,2}$ dimers and trimers are found to have a simple structure in which the rare gas atom is located on the C_6 symmetry axis of the benzene monomer. Depending on the species the rare gas atom is found to be located at a distance of $3.4 - 3.8$ Å from the plane of the benzene molecule. For the trimer the rare gas atoms are localized on the C_6 symmetry axis, symmetrically on the opposite sides of the benzene plane. The dimer formation reduces the point group symmetry from D_{6h} symmetry for the benzene monomer to C_{6v} and the trimer symmetry is same as the monomer. The results provided a benchmark for refining the potential energy surfaces which describe the intermolecular forces acting between the monomers.

In the future, higher complexes (tetramer, pentamer etc.) can be observed with benzene being soluted by noble gas atoms. The behaviour of Fermi resonance phenomena with the formation of larger complexes need to be further investigated. The high-resolution measurements can also be extended to larger planar aromatic molecules. To observe higher complexes it is required to rotationally cool the molecules to less than 1 K. For the present set-up this might be possible by further cooling the gas before the cluster formation, U. Evan et al. [42] achieved this by implementing a specially designed high pressure valve with miniaturized valve parts.

The benzene - rare gas trimer observed in this study was 12 times weaker than the monomer (benzene) spectral lines. The line strength decreases with the size of the complexes. To observe weaker lines the sensitivity of the system must be improved. One way is to increase the path length of the multipass absorption cell. The multipass cell used in our spectrometer (Aerodyne Research Inc., AMAC-100) is aligned to provide 182 laser passes. McManus [43]

showed that by changing the separation between the mirrors and rotation about the optical axis, the number of passes can be increased to 274 or 366. This will increase the effective absorption path length in the system and should provide higher signal to noise ratio.

The resolution of the obtained spectra from the current set-up was ~ 60 MHz. To observe the larger complexes it is required to improve the resolution. As the size of the complexes, the band origin of the complexes tend to shift with respect to the monomer band origin, as shown in Table 4.5, this shift is very small and one needs to increase the resolution of the system to observe this shift. The laser line width of the OPO is less than 1 MHz, so it is possible to further increase the resolution. The residual Doppler broadening can be decreased by implementing a skimmer [45].

Bibliography

[1] P. R. Bunker and P. Jensen, *Molecular Symmetry and Spectroscopy*, NRC Research Press, Ottawa, 2nd edition (1998).

[2] D. Papoušek and M. R. Aliev, *Molecular Vibrational-Rotational Spectra*, Elsevier Scientific Publishing Co., Amsterdam/Oxford/New York, (1982).

[3] P. R. Bunker and P. Jensen, *Fundamentals of Molecular Symmetry*, Institute of Physics Publishing, Bristol/Philadelphia, (2005).

[4] H. C. Allen and P. C. Cross, *Molecular Vib-Rotors*, Elsevier Scientific Publishing Co., New York and London, (1963).

[5] W. Demtröder, *Molecular Physics - Theoretical Principles and Experimental Methodes*, WILEY-VCH, (2003).

[6] R. N. Zare, *Angular Momentum: Understanding Spatial Aspects in Chemistry and Physics*, Wiley, New York (1988).

[7] W. Gordy and R. L. Cook, *Microwave Molecular Spectra*, Wiley, (1984).

[8] D. J. Willock, *Molecular Symmetry*, Wiley, (2009).

[9] B. K. Shivamoggi, *Theoretical Fluid Mechanics*, Wiley, (1998).

[10] M. V. Johnston, *Trends Anal. Chem.*, vol. 3, no.2 (1984).

[11] H. J. Neusser, R. Sussman, *Jet Spectroscopy and Molecular Dynamics*, eds. J. M. Hollas, D. Phillips, Springer Media, New York (1995) 118.

[12] M. Rezaei, *High-Resolution Pulsed Slit Jet Spectrometer with QCL and OPO probes for Infrared Spectroscopy on van der Waals Clusters*, PhD Thesis, University of Calgary (2014).

[13] J. N. Oliaee, *High Resolution Infrared Spectroscopy of van der Waals Clusters of Nitrous Oxide, Carbon Dioxide and OCS-R Complexes*, PhD Thesis, University of Calgary (2013).

[14] S. M. Beck, M. G. Liverman, D. L. Monts, R. E. Smalley, J. Chem. Phys. **70**, 232 (1979).

[15] R. E. Smalley, L. Wharton and D. H. Levy, Acc. Chem. Res. **10**, 139 (1977).

[16] J. Koperski and E. S. Fry, J. Phys. B: At. Mol. Opt. Phys. **39**, 1125 (2006).

[17] M. Hayashi, Y. Ohshima, Chem. Phys. **419**, 131 (2013).

[18] D. M. Lubman, C. Retiner and R. N. Zare, J. Phys. Chem. **86**, 1129 (1982).

[19] T. Weber, E. Riedle, H. J. Neusser, E. W. Schlag, J. Mol. Structure **249**, 69 (1991).

[20] H. J. Neusser, R. Sussman, A. M. Smith, E. Riedle, T. Weber, Ber. Bunsenges. Phys. Chem. **96**, 1252 (1992).

[21] T. Weber, A. Von Bargen, E. Riedle, H. J. Neusser, J. Chem. Phys. **92**, 90 (1990).

[22] R. Sussmann, R. Neuhauser, H. J. Neusser, J. Chem. Phys. **103**, 3315 (1995).

[23] R. Neuhauser, J. Braun, H. J. Neusser, A. van der Avoird, J. Chem. Phys. **108**, 8408 (1998) .

[24] T. Weber, E. Riedle, H. J. Neusser, E. W. Schlag, Chem. Phys. Lett. **183**, 77 (1991).

[25] S. Lee, J.S. Chung, P. M. Felker, J. L. Cacheiro, B. Fernández, T. B. Pedersen, H. Koch, J. Chem. Phys. **119**, 12956 (2003).

[26] W. Kim, P. M. Felker, J. Chem. Phys. **107**, 2193 (1997).

[27] E. Arunan, T. Emilsson, H.S. Gutowksy, J. Chem. Phys. **101**, 861 (1994).

[28] T. Brupbacher, J. Makarewicz, A. Bauder, J. Chem. Phys. **101**, 9736 (1994).

[29] T. Brupbacher, A. Bauder, Chem. Phys. Lett. **173**, 435 (1990).

[30] T. D. Klots, T. Emilsson, H. S. Gutowsky, J. Chem. Phys. **97**, 5335 (1992).

[31] J. Plíva, J.W.C. Johns, L. Goodman, J. Mol. Spectrosc. **163**, 108 (1994).

[32] M. Rezaei, A.R.W. McKellar, N. Moazzen-Ahmadi, J. Mol. Spectrosc. 296 (2014) 14.

[33] M. Dehghani, M. Afshari, Z. Abusara, N. Moazzen-Ahmadi, A.R.W. McKellar, J. Chem. Phys. **126**, 164310 (2007).

[34] N. Moazzen-Ahmadi, A.R.W. McKellar, Int. Rev. Phys. Chem. **32**, 611 (2013).

[35] C. M. Western, *a program for simulating rotational structure* PGOPHER, University of Bristol, UK; See `http://pgopher.chm.bris.ac.uk`.

[36] J. Plíva, A. Valentin, J. Chazelas, L. Henry, J. Mol. Spectrosc. **134** 220 (1989).

[37] S. B. Capelo, B. Fernández, H. Koch, P. M. Felker, J. Phys. Chem. A **113**, 5212 (2009).

[38] W. Chen, G. Mouret, D. Boucher, Appl. Phys. B **67**, 375 (1998).

[39] M Vainio, M. Siltanen, J. Peltola, L. Halonen, Appl. Opt. **50**, 4 (2010).

[40] O. F. Hagena, and W. Obert, J. Chem. Phys. **56**, 1793 (1972).

[41] J. B. Hopkins, P.R. Langridge-Smith, M. D. Morse, and R. E. Smalley, J. Chem. Phys. **78**, 1627 (1983).

[42] U. Evan, J. Jortner, D. Noy, N. Lavie, and C. Cossart-MagosChem, J. Chem. Phys. **112**, 8068 (2000).

[43] J. B. McManus, P. L. Kebabian, and M. S. Zahniser, Appl. Opt. **34**, 3336 (1995).

[44] Z. Kisiel, http://www.ifpan.edu.pl/ kisiel/struct/struct.htm

[45] R. Campargue, Rev. Sci. Instrum. **35** , 111 (1964).

[46] J. George, A. R. W McKellar, and N. Moazzen-Ahmadi, Chem. Phys. Lett. **610**, 121 (2014).

Appendix A

Supplementary data for Chapter 4

Dimer Complexes

Calculated and observed transitions for C_6D_6−He, C_6D_6−Ne and C_6D_6−Ar dimers.

Table A.1: Observed transitions in the $\nu_2 + \nu_{13}$ ($\sim$ 2275 cm^{-1}) and ν_{12} ($\sim$ 2288 cm^{-1}) bands of C_6D_6−He (values in cm^{-1}).

J'	K'	L'	J''	K''	Observed	Calculated	Obs.-Calc.
6	6	-1	7	7	2274.5093	2274.5094	-0.0001
5	3	-1	6	4	2274.7128	2274.7118	0.0010
5	4	-1	6	5	2274.7170	2274.7163	0.0007
5	5	-1	6	6	2274.7206	2274.7209	-0.0003
5	5	-1	6	6	2274.7206	2274.7209	-0.0003
4	1	-1	5	2	2274.9189	2274.9192	-0.0003
4	2	-1	5	3	2274.9242	2274.9237	0.0005
4	2	-1	5	3	2274.9242	2274.9237	0.0005
4	3	-1	5	4	2274.9281	2274.9280	0.0001
4	4	-1	5	5	2274.9322	2274.9323	0.0000
3	0		4	1	2275.1297	2275.1305	-0.0008
3	1	-1	4	2	2275.1344	2275.1350	-0.0007
3	2	-1	4	3	2275.1397	2275.1394	0.0003
3	2	-1	4	3	2275.1397	2275.1394	0.0003
3	3	-1	4	4	2275.1432	2275.1435	-0.0003
2	1	1	3	0	2275.3411	2275.3413	-0.0002
2	0		3	1	2275.3455	2275.3458	-0.0004
2	1	-1	3	2	2275.3503	2275.3504	-0.0001
2	2	-1	3	3	2275.3548	2275.3546	0.0002
2	2	-1	3	3	2275.3548	2275.3546	0.0002
1	0		2	1	2275.5612	2275.5610	0.0002
1	1	-1	2	2	2275.5658	2275.5655	0.0003
0	0		1	1	2275.7765	2275.7761	0.0005
5	4	1	5	3	2275.9699	2275.9689	0.0010
7	2	1	7	1	2275.9699	2275.9706	-0.0007

J'	K'	L'	J''	K''	Observed	Calculated	Obs.-Calc.
4	4	1	4	3	2275.9699	2275.9700	-0.0001
5	4	1	5	3	2275.9699	2275.9689	0.0010
6	3	1	6	2	2275.9699	2275.9711	-0.0012
4	4	1	4	3	2275.9699	2275.9700	-0.0001
4	3	1	4	2	2275.9752	2275.9753	-0.0001
6	2	1	6	1	2275.9752	2275.9756	-0.0004
3	3	1	3	2	2275.9752	2275.9759	-0.0007
2	2	1	2	1	2275.9807	2275.9813	-0.0006
4	2	1	4	1	2275.9807	2275.9803	0.0004
3	2	1	3	1	2275.9807	2275.9811	-0.0004
4	1	1	4	0	2275.9857	2275.9844	0.0013
1	1	1	1	0	2275.9857	2275.9863	-0.0006
2	1	1	2	0	2275.9857	2275.9861	-0.0004
3	1	1	3	0	2275.9857	2275.9856	0.0002
1	0		1	1	2275.9911	2275.9912	-0.0001
3	0		3	1	2275.9911	2275.9909	0.0002
2	0		2	1	2275.9911	2275.9912	-0.0001
4	0		4	1	2275.9911	2275.9902	0.0009
3	1	-1	3	2	2275.9951	2275.9954	-0.0003
2	1	-1	2	2	2275.9951	2275.9957	-0.0005
4	1	-1	4	2	2275.9951	2275.9947	0.0004
6	3	-1	6	4	2275.9991	2275.9998	-0.0007
4	2	-1	4	3	2275.9991	2275.9991	0.0000
4	2	-1	4	3	2275.9991	2275.9991	0.0000
3	2	-1	3	3	2275.9991	2275.9997	-0.0007
3	2	-1	3	3	2275.9991	2275.9997	-0.0007
1	1	1	0	0	2276.2020	2276.2016	0.0003
2	2	1	1	1	2276.4119	2276.4116	0.0003
2	1	1	1	0	2276.4171	2276.4169	0.0002
2	0		1	1	2276.4216	2276.4214	0.0001
3	3	1	2	2	2276.6218	2276.6212	0.0007
3	2	1	2	1	2276.6267	2276.6264	0.0002
3	1	1	2	0	2276.6319	2276.6320	-0.0002
3	0		2	1	2276.6365	2276.6363	0.0002
4	4	1	3	3	2276.8309	2276.8304	0.0005
4	4	1	3	3	2276.8309	2276.8304	0.0005

J'	K'	L'	J''	K''	Observed	Calculated	Obs.-Calc.
4	3	1	3	2	2276.8357	2276.8357	0.0000
4	2	1	3	1	2276.8404	2276.8408	-0.0004
4	1	1	3	0	2276.8467	2276.8467	0.0000
4	0		3	1	2276.8503	2276.8506	-0.0003
4	1	-1	3	2	2276.8554	2276.8551	0.0002
5	5	1	4	4	2277.0397	2277.0392	0.0005
5	4	1	4	3	2277.0441	2277.0444	-0.0002
5	4	1	4	3	2277.0441	2277.0444	-0.0002
5	3	1	4	2	2277.0490	2277.0494	-0.0004
5	2	1	4	1	2277.0538	2277.0542	-0.0004
5	1	1	4	0	2277.0607	2277.0606	0.0000
5	0		4	1	2277.0642	2277.0641	0.0001
5	1	-1	4	2	2277.0690	2277.0687	0.0003
6	6	1	5	5	2277.2475	2277.2476	-0.0001
6	5	1	5	4	2277.2516	2277.2523	-0.0007
6	4	1	5	3	2277.2564	2277.2571	-0.0007
6	4	1	5	3	2277.2564	2277.2571	-0.0007
6	3	1	5	2	2277.2615	2277.2617	-0.0002
6	2	1	5	1	2277.2660	2277.2663	-0.0002
7	7	1	6	6	2277.4555	2277.4556	-0.0001
7	7	1	6	6	2277.4555	2277.4556	-0.0001
7	6	1	6	5	2277.4592	2277.4596	-0.0004
7	5	1	6	4	2277.4639	2277.4638	0.0001
7	4	1	6	3	2277.4685	2277.4680	0.0005
7	4	1	6	3	2277.4685	2277.4680	0.0005
7	3	1	6	2	2277.4734	2277.4722	0.0012
8	8	1	7	7	2277.6633	2277.6632	0.0001
8	7	1	7	6	2277.6663	2277.6662	0.0001
8	7	1	7	6	2277.6663	2277.6662	0.0001
4	3	-1	5	4	2287.7743	2287.7743	0.0000
4	4	-1	5	5	2287.8036	2287.8040	-0.0004
3	1	-1	4	2	2287.9295	2287.9309	-0.0014
3	2	-1	4	3	2287.9600	2287.9603	-0.0003
3	2	-1	4	3	2287.9600	2287.9603	-0.0003
3	3	-1	4	4	2287.9898	2287.9897	0.0001
2	0		3	1	2288.1161	2288.1165	-0.0005

J'	K'	L'	J''	K''	Observed	Calculated	Obs.-Calc.
2	1	-1	3	2	2288.1459	2288.1461	-0.0001
2	2	-1	3	3	2288.1757	2288.1754	0.0003
2	2	-1	3	3	2288.1757	2288.1754	0.0003
1	1	1	2	0	2288.3017	2288.3018	-0.0001
1	0		2	1	2288.3317	2288.3316	0.0001
1	1	-1	2	2	2288.3615	2288.3611	0.0004
0	0		1	1	2288.5467	2288.5466	0.0002
3	3	1	3	2	2288.6712	2288.6722	-0.0009
5	3	1	5	2	2288.6712	2288.6705	0.0008
4	3	1	4	2	2288.6712	2288.6717	-0.0004
4	2	1	4	1	2288.7024	2288.7016	0.0008
3	2	1	3	1	2288.7024	2288.7021	0.0003
2	2	1	2	1	2288.7024	2288.7022	0.0002
3	1	1	3	0	2288.7320	2288.7321	-0.0001
4	1	1	4	0	2288.7320	2288.7316	0.0004
2	1	1	2	0	2288.7320	2288.7321	-0.0002
1	1	1	1	0	2288.7320	2288.7321	-0.0001
3	0		3	1	2288.7621	2288.7618	0.0003
4	0		4	1	2288.7621	2288.7614	0.0007
2	0		2	1	2288.7621	2288.7619	0.0002
1	0		1	1	2288.7621	2288.7618	0.0003
4	1	-1	4	2	2288.7914	2288.7909	0.0005
3	1	-1	3	2	2288.7914	2288.7913	0.0001
2	1	-1	2	2	2288.7914	2288.7914	0.0000
4	3	-1	4	4	2288.8494	2288.8497	-0.0003
5	3	-1	5	4	2288.8494	2288.8486	0.0008
2	2	1	1	1	2289.1329	2289.1324	0.0004
2	1	1	1	0	2289.1627	2289.1624	0.0003
3	2	1	2	1	2289.3468	2289.3475	-0.0007
3	1	1	2	0	2289.3770	2289.3774	-0.0004
3	0		2	1	2289.4068	2289.4072	-0.0004
5	5	1	4	4	2289.6875	2289.6869	0.0006
5	4	1	4	3	2289.7161	2289.7162	0.0000
5	4	1	4	3	2289.7161	2289.7162	0.0000
5	3	1	4	2	2289.7456	2289.7460	-0.0004
5	2	1	4	1	2289.7752	2289.7760	-0.0007

J'	K'	L'	J''	K''	Observed	Calculated	Obs.-Calc.
6	6	1	5	5	2289.8715	2289.8713	0.0001
6	5	1	5	4	2289.9000	2289.8996	0.0003
6	4	1	5	3	2289.9287	2289.9289	-0.0001
6	4	1	5	3	2289.9287	2289.9289	-0.0001
6	3	1	5	2	2289.9584	2289.9587	-0.0003
7	7	1	6	6	2290.0556	2290.0557	-0.0001
7	7	1	6	6	2290.0556	2290.0557	-0.0001

Table A.2: Observed transitions in the $\nu_2 + \nu_{13}$ and ν_{12} bands of C_6D_6−Ne.

J'	K'	L'	J''	K''	Observed	Calculated	Obs.-Calc.
5	5	-1	6	6	2274.7295	2274.7303	-0.0007
5	5	-1	6	6	2274.7295	2274.7303	-0.0007
4	4	-1	5	5	2274.9418	2274.9413	0.0004
5	2	-1	6	3	2275.0301	2275.0276	0.0025
5	2	-1	6	3	2275.0301	2275.0276	0.0025
4	3	-1	5	4	2275.0393	2275.0405	-0.0012
3	3	-1	4	4	2275.1530	2275.1525	0.0005
4	1	-1	5	2	2275.2361	2275.2384	-0.0023
3	2	-1	4	3	2275.2513	2275.2516	-0.0003
3	2	-1	4	3	2275.2513	2275.2516	-0.0003
2	2	-1	3	3	2275.3644	2275.3637	0.0007
2	2	-1	3	3	2275.3644	2275.3637	0.0007
1	1	-1	2	2	2275.5750	2275.5749	0.0001
1	1	-1	2	2	2275.5750	2275.5749	0.0001
9	3	-1	9	4	2275.6017	2275.6024	-0.0006
6	3	-1	6	4	2275.6017	2275.6017	0.0001
4	3	-1	4	4	2275.6017	2275.6014	0.0004
7	3	-1	7	4	2275.6017	2275.6019	-0.0001
5	3	-1	5	4	2275.6017	2275.6015	0.0002
8	3	-1	8	4	2275.6017	2275.6021	-0.0004
10	3	-1	10	4	2275.6017	2275.6027	-0.0009
1	0		2	1	2275.6746	2275.6737	0.0009
4	2	-1	4	3	2275.7009	2275.7005	0.0003
6	2	-1	6	3	2275.7009	2275.7008	0.0001
5	2	-1	5	3	2275.7009	2275.7006	0.0002
7	2	-1	7	3	2275.7009	2275.7009	0.0000
8	2	-1	8	3	2275.7009	2275.7010	-0.0002
8	2	-1	8	3	2275.7009	2275.7010	-0.0002
4	2	-1	4	3	2275.7009	2275.7005	0.0003
6	2	-1	6	3	2275.7009	2275.7008	0.0001
5	2	-1	5	3	2275.7009	2275.7006	0.0002
7	2	-1	7	3	2275.7009	2275.7009	0.0000
9	1	-1	9	2	2275.7998	2275.7999	0.0000
10	1	-1	10	2	2275.7998	2275.8000	-0.0001
6	1	-1	6	2	2275.7998	2275.7996	0.0002

J'	K'	L'	J''	K''	Observed	Calculated	Obs.-Calc.
5	1	-1	5	2	2275.7998	2275.7996	0.0002
3	1	-1	3	2	2275.7998	2275.7995	0.0003
8	1	-1	8	2	2275.7998	2275.7998	0.0000
4	1	-1	4	2	2275.7998	2275.7995	0.0003
7	1	-1	7	2	2275.7998	2275.7997	0.0001
7	0		7	1	2275.8984	2275.8983	0.0001
9	0		9	1	2275.8984	2275.8983	0.0001
8	0		8	1	2275.8984	2275.8983	0.0001
10	0		10	1	2275.8984	2275.8983	0.0001
6	0		6	1	2275.8984	2275.8983	0.0001
5	0		5	1	2275.8984	2275.8983	0.0001
3	0		3	1	2275.8984	2275.8983	0.0001
4	0		4	1	2275.8984	2275.8983	0.0001
3	1	1	3	0	2275.9962	2275.9969	-0.0007
6	1	1	6	0	2275.9962	2275.9967	-0.0005
9	1	1	9	0	2275.9962	2275.9965	-0.0003
7	1	1	7	0	2275.9962	2275.9967	-0.0004
4	1	1	4	0	2275.9962	2275.9968	-0.0006
8	1	1	8	0	2275.9962	2275.9966	-0.0004
10	1	1	10	0	2275.9962	2275.9964	-0.0002
5	1	1	5	0	2275.9962	2275.9968	-0.0006
3	2	1	3	1	2276.0947	2276.0952	-0.0005
2	2	1	2	1	2276.0947	2276.0953	-0.0006
9	2	1	9	1	2276.0947	2276.0945	0.0002
10	2	1	10	1	2276.0947	2276.0943	0.0004
7	2	1	7	1	2276.0947	2276.0948	-0.0001
4	2	1	4	1	2276.0947	2276.0952	-0.0004
5	2	1	5	1	2276.0947	2276.0951	-0.0003
6	2	1	6	1	2276.0947	2276.0950	-0.0002
1	1	1	0	0	2276.1099	2276.1092	0.0006
2	1	1	1	0	2276.2219	2276.2215	0.0004
3	0		2	1	2276.2356	2276.2351	0.0004
3	2	1	2	1	2276.4306	2276.4321	-0.0015
4	1	1	3	0	2276.4435	2276.4459	-0.0024
3	3	1	2	2	2276.5264	2276.5302	-0.0038
4	2	1	3	1	2276.5374	2276.5442	-0.0068

J'	K'	L'	J''	K''	Observed	Calculated	Obs.-Calc.
4	3	1	3	2	2276.6475	2276.6423	0.0053
5	2	1	4	1	2276.6595	2276.6563	0.0032
4	4	1	3	3	2276.7413	2276.7401	0.0012
4	4	1	3	3	2276.7413	2276.7401	0.0012
5	3	1	4	2	2276.7547	2276.7543	0.0004
6	2	1	5	1	2276.7698	2276.7683	0.0016
5	4	1	4	3	2276.8493	2276.8520	-0.0027
5	4	1	4	3	2276.8493	2276.8520	-0.0027
6	3	1	5	2	2276.8676	2276.8662	0.0015
5	5	1	4	4	2276.9490	2276.9495	-0.0005
6	4	1	5	3	2276.9654	2276.9638	0.0016
6	4	1	5	3	2276.9654	2276.9638	0.0016
7	3	1	6	2	2276.9795	2276.9780	0.0015
6	5	1	5	4	2277.0641	2277.0612	0.0029
6	6	1	5	5	2277.1568	2277.1583	-0.0015
7	5	1	6	4	2277.1733	2277.1728	0.0005
8	4	1	7	3	2277.1865	2277.1871	-0.0006
8	4	1	7	3	2277.1865	2277.1871	-0.0006
9	3	-1	10	4	2287.3077	2287.3084	-0.0008
7	6	-1	8	7	2287.3077	2287.3093	-0.0016
8	2	-1	9	3	2287.4937	2287.4936	0.0001
8	2	-1	9	3	2287.4937	2287.4936	0.0001
6	5	-1	7	6	2287.4937	2287.4950	-0.0013
6	5	-1	7	6	2287.4937	2287.4950	-0.0013
7	3	-1	8	4	2287.5311	2287.5315	-0.0004
6	4	-1	7	5	2287.5692	2287.5691	0.0001
8	1	-1	9	2	2287.5692	2287.5672	0.0020
5	5	-1	6	6	2287.6069	2287.6066	0.0003
7	2	-1	8	3	2287.6069	2287.6053	0.0016
5	5	-1	6	6	2287.6069	2287.6066	0.0003
7	2	-1	8	3	2287.6069	2287.6053	0.0016
6	3	-1	7	4	2287.6426	2287.6432	-0.0006
5	4	-1	6	5	2287.6807	2287.6809	-0.0001
7	1	-1	8	2	2287.6807	2287.6790	0.0017
4	4	-1	5	5	2287.7926	2287.7927	-0.0001
5	2	-1	6	3	2287.8291	2287.8290	0.0000

J'	K'	L'	J''	K''	Observed	Calculated	Obs.-Calc.
5	2	-1	6	3	2287.8291	2287.8290	0.0000
4	3	-1	5	4	2287.8671	2287.8669	0.0002
5	1	-1	6	2	2287.9028	2287.9029	-0.0002
4	2	-1	5	3	2287.9403	2287.9410	-0.0008
4	2	-1	5	3	2287.9403	2287.9410	-0.0008
3	2	-1	4	3	2288.0538	2288.0531	0.0006
3	2	-1	4	3	2288.0538	2288.0531	0.0006
4	0		5	1	2288.0903	2288.0888	0.0015
7	5	-1	7	6	2288.2808	2288.2794	0.0014
11	5	-1	11	6	2288.2808	2288.2810	-0.0001
7	5	-1	7	6	2288.2808	2288.2794	0.0014
8	5	-1	8	6	2288.2808	2288.2797	0.0011
8	5	-1	8	6	2288.2808	2288.2797	0.0011
10	5	-1	10	6	2288.2808	2288.2805	0.0003
11	5	-1	11	6	2288.2808	2288.2810	-0.0001
9	5	-1	9	6	2288.2808	2288.2801	0.0007
9	5	-1	9	6	2288.2808	2288.2801	0.0007
10	5	-1	10	6	2288.2808	2288.2805	0.0003
7	4	-1	7	5	2288.3536	2288.3539	-0.0003
6	4	-1	6	5	2288.3536	2288.3537	-0.0001
9	4	-1	9	5	2288.3536	2288.3544	-0.0009
10	4	-1	10	5	2288.3536	2288.3547	-0.0012
1	1	-1	2	2	2288.3536	2288.3516	0.0020
12	4	-1	12	5	2288.3536	2288.3554	-0.0019
11	4	-1	11	5	2288.3536	2288.3551	-0.0015
8	4	-1	8	5	2288.3536	2288.3541	-0.0006
5	4	-1	5	5	2288.3536	2288.3535	0.0001
11	3	-1	11	4	2288.4285	2288.4290	-0.0005
10	3	-1	10	4	2288.4285	2288.4288	-0.0002
9	3	-1	9	4	2288.4285	2288.4285	0.0000
13	3	-1	13	4	2288.4285	2288.4295	-0.0010
7	3	-1	7	4	2288.4285	2288.4282	0.0004
6	3	-1	6	4	2288.4285	2288.4280	0.0005
8	3	-1	8	4	2288.4285	2288.4283	0.0002
5	3	-1	5	4	2288.4285	2288.4279	0.0006
4	3	-1	4	4	2288.4285	2288.4278	0.0007

J'	K'	L'	J''	K''	Observed	Calculated	Obs.-Calc.
12	3	-1	12	4	2288.4285	2288.4292	-0.0007
6	1	-1	6	2	2288.5765	2288.5762	0.0004
4	1	-1	4	2	2288.5765	2288.5761	0.0004
8	1	-1	8	2	2288.5765	2288.5762	0.0003
3	1	-1	3	2	2288.5765	2288.5761	0.0004
11	1	-1	11	2	2288.5765	2288.5763	0.0003
5	1	-1	5	2	2288.5765	2288.5761	0.0004
10	1	-1	10	2	2288.5765	2288.5762	0.0003
7	1	-1	7	2	2288.5765	2288.5762	0.0004
9	1	-1	9	2	2288.5765	2288.5762	0.0003
2	1	-1	2	2	2288.5765	2288.5761	0.0004
1	0		1	1	2288.6497	2288.6501	-0.0004
9	0		9	1	2288.6497	2288.6498	0.0000
3	0		3	1	2288.6497	2288.6501	-0.0003
8	0		8	1	2288.6497	2288.6498	-0.0001
2	0		2	1	2288.6497	2288.6501	-0.0004
5	0		5	1	2288.6497	2288.6500	-0.0003
6	0		6	1	2288.6497	2288.6499	-0.0002
4	0		4	1	2288.6497	2288.6500	-0.0003
7	0		7	1	2288.6497	2288.6499	-0.0002
10	0		10	1	2288.6497	2288.6497	0.0000
6	1	1	6	0	2288.7229	2288.7235	-0.0006
10	1	1	10	0	2288.7229	2288.7230	0.0000
1	1	1	1	0	2288.7229	2288.7239	-0.0009
3	1	1	3	0	2288.7229	2288.7238	-0.0008
5	1	1	5	0	2288.7229	2288.7236	-0.0007
9	1	1	9	0	2288.7229	2288.7231	-0.0002
2	1	1	2	0	2288.7229	2288.7238	-0.0009
4	1	1	4	0	2288.7229	2288.7237	-0.0008
7	1	1	7	0	2288.7229	2288.7234	-0.0005
8	1	1	8	0	2288.7229	2288.7233	-0.0003
11	2	1	11	1	2288.7964	2288.7957	0.0007
5	2	1	5	1	2288.7964	2288.7971	-0.0007
9	2	1	9	1	2288.7964	2288.7963	0.0001
8	2	1	8	1	2288.7964	2288.7965	-0.0001
3	2	1	3	1	2288.7964	2288.7973	-0.0009

J'	K'	L'	J''	K''	Observed	Calculated	Obs.-Calc.
6	2	1	6	1	2288.7964	2288.7969	-0.0005
4	2	1	4	1	2288.7964	2288.7972	-0.0008
7	2	1	7	1	2288.7964	2288.7968	-0.0003
2	2	1	2	1	2288.7964	2288.7974	-0.0010
10	2	1	10	1	2288.7964	2288.7960	0.0004
10	3	1	10	2	2288.8695	2288.8689	0.0006
9	3	1	9	2	2288.8695	2288.8693	0.0002
12	3	1	12	2	2288.8695	2288.8681	0.0014
3	3	1	3	2	2288.8695	2288.8707	-0.0012
11	3	1	11	2	2288.8695	2288.8685	0.0010
5	3	1	5	2	2288.8695	2288.8704	-0.0009
7	3	1	7	2	2288.8695	2288.8699	-0.0004
8	3	1	8	2	2288.8695	2288.8696	-0.0001
6	3	1	6	2	2288.8695	2288.8702	-0.0007
4	3	1	4	2	2288.8695	2288.8706	-0.0011
4	3	1	3	2	2289.3198	2289.3195	0.0003
4	4	1	3	3	2289.3935	2289.3926	0.0009
4	4	1	3	3	2289.3935	2289.3926	0.0009
5	3	1	4	2	2289.4319	2289.4315	0.0004
5	5	1	4	4	2289.5783	2289.5772	0.0011

Table A.3: Observed transitions in the $\nu_2 + \nu_{13}$ and ν_{12} bands of C_6D_6−Ar.

J'	K'	L'	J''	K''	Observed	Calculated	Obs.-Calc.
6	3	-1	7	4	2274.8808	2274.8802	0.0006
4	4	-1	5	5	2274.8926	2274.8918	0.0008
7	2	-1	8	3	2274.9421	2274.9425	-0.0005
7	2	-1	8	3	2274.9421	2274.9425	-0.0005
5	3	-1	6	4	2274.9546	2274.9544	0.0001
4	3	-1	5	4	2275.0292	2275.0286	0.0005
7	1	-1	8	2	2275.0792	2275.0787	0.0005
5	2	-1	6	3	2275.0917	2275.0909	0.0008
5	2	-1	6	3	2275.0917	2275.0909	0.0008
3	3	-1	4	4	2275.1033	2275.1029	0.0004
6	1	-1	7	2	2275.1528	2275.1529	-0.0001
4	2	-1	5	3	2275.1655	2275.1652	0.0003
4	2	-1	5	3	2275.1655	2275.1652	0.0003
3	2	-1	4	3	2275.2396	2275.2394	0.0002
3	2	-1	4	3	2275.2396	2275.2394	0.0002
8	4	-1	8	5	2275.2628	2275.2626	0.0002
7	4	-1	7	5	2275.2628	2275.2626	0.0002
6	4	-1	6	5	2275.2628	2275.2626	0.0002
9	4	-1	9	5	2275.2628	2275.2626	0.0002
5	4	-1	5	5	2275.2628	2275.2627	0.0001
10	4	-1	10	5	2275.2628	2275.2627	0.0001
10	2	1	11	1	2275.2628	2275.2627	0.0001
11	4	-1	11	5	2275.2628	2275.2629	-0.0001
12	4	-1	12	5	2275.2628	2275.2631	-0.0003
13	4	-1	13	5	2275.2628	2275.2634	-0.0006
8	1	1	9	0	2275.2760	2275.2758	0.0002
6	0		7	1	2275.2888	2275.2887	0.0001
4	1	-1	5	2	2275.3018	2275.3014	0.0005
2	2	-1	3	3	2275.3142	2275.3136	0.0005
2	2	-1	3	3	2275.3142	2275.3136	0.0005
5	0		6	1	2275.3631	2275.3630	0.0001
3	1	-1	4	2	2275.3757	2275.3756	0.0001
2	1	-1	3	2	2275.4498	2275.4499	0.0000
5	1	1	6	0	2275.4983	2275.4985	-0.0002
3	0		4	1	2275.5112	2275.5115	-0.0003

J'	K'	L'	J''	K''	Observed	Calculated	Obs.-Calc.
1	1	-1	2	2	2275.5242	2275.5241	0.0001
8	2	-1	8	3	2275.5352	2275.5360	-0.0008
8	2	-1	8	3	2275.5352	2275.5360	-0.0008
7	2	-1	7	3	2275.5352	2275.5360	-0.0008
7	2	-1	7	3	2275.5352	2275.5360	-0.0008
6	2	-1	6	3	2275.5352	2275.5360	-0.0008
6	2	-1	6	3	2275.5352	2275.5360	-0.0008
5	2	-1	5	3	2275.5352	2275.5361	-0.0009
5	2	-1	5	3	2275.5352	2275.5361	-0.0009
4	2	-1	4	3	2275.5352	2275.5361	-0.0009
4	2	-1	4	3	2275.5352	2275.5361	-0.0009
4	1	1	5	0	2275.5727	2275.5728	-0.0001
2	0		3	1	2275.5860	2275.5858	0.0002
1	0		2	1	2275.6602	2275.6600	0.0002
9	1	-1	9	2	2275.6724	2275.6721	0.0002
8	1	-1	8	2	2275.6724	2275.6722	0.0002
7	1	-1	7	2	2275.6724	2275.6722	0.0002
10	1	-1	10	2	2275.6724	2275.6722	0.0002
6	1	-1	6	2	2275.6724	2275.6722	0.0001
11	1	-1	11	2	2275.6724	2275.6723	0.0001
5	1	-1	5	2	2275.6724	2275.6723	0.0001
4	1	-1	4	2	2275.6724	2275.6724	0.0000
3	1	-1	3	2	2275.6724	2275.6724	-0.0001
2	1	-1	2	2	2275.6724	2275.6725	-0.0001
9	0		9	1	2275.8083	2275.8080	0.0004
8	0		8	1	2275.8083	2275.8080	0.0003
10	0		10	1	2275.8083	2275.8080	0.0003
7	0		7	1	2275.8083	2275.8080	0.0003
6	0		6	1	2275.8083	2275.8081	0.0002
5	0		5	1	2275.8083	2275.8082	0.0002
4	0		4	1	2275.8083	2275.8083	0.0001
3	0		3	1	2275.8083	2275.8083	0.0000
2	0		2	1	2275.8083	2275.8084	0.0000
1	0		1	1	2275.8083	2275.8084	-0.0001
9	1	1	9	0	2275.9437	2275.9435	0.0002
10	1	1	10	0	2275.9437	2275.9435	0.0002

J'	K'	L'	J''	K''	Observed	Calculated	Obs.-Calc.
8	1	1	8	0	2275.9437	2275.9435	0.0002
7	1	1	7	0	2275.9437	2275.9436	0.0001
6	1	1	6	0	2275.9437	2275.9437	0.0000
5	1	1	5	0	2275.9437	2275.9437	0.0000
4	1	1	4	0	2275.9437	2275.9438	-0.0001
3	1	1	3	0	2275.9437	2275.9439	-0.0002
2	1	1	2	0	2275.9437	2275.9440	-0.0003
1	1	1	1	0	2275.9437	2275.9440	-0.0003
10	2	1	10	1	2276.0788	2276.0786	0.0002
9	2	1	9	1	2276.0788	2276.0786	0.0002
11	2	1	11	1	2276.0788	2276.0786	0.0002
8	2	1	8	1	2276.0788	2276.0787	0.0001
7	2	1	7	1	2276.0788	2276.0788	0.0000
6	2	1	6	1	2276.0788	2276.0789	0.0000
5	2	1	5	1	2276.0788	2276.0790	-0.0001
4	2	1	4	1	2276.0788	2276.0791	-0.0002
3	2	1	3	1	2276.0788	2276.0791	-0.0003
2	2	1	2	1	2276.0788	2276.0792	-0.0004
2	1	1	1	0	2276.0925	2276.0924	0.0001
4	0		3	1	2276.1051	2276.1051	0.0000
10	3	1	10	2	2276.2136	2276.2134	0.0002
11	3	1	11	2	2276.2136	2276.2134	0.0002
9	3	1	9	2	2276.2136	2276.2134	0.0001
12	3	1	12	2	2276.2136	2276.2135	0.0001
8	3	1	8	2	2276.2136	2276.2135	0.0000
7	3	1	7	2	2276.2136	2276.2136	-0.0001
6	3	1	6	2	2276.2136	2276.2137	-0.0002
5	3	1	5	2	2276.2136	2276.2139	-0.0003
4	3	1	4	2	2276.2136	2276.2140	-0.0004
3	3	1	3	2	2276.2136	2276.2141	-0.0005
2	2	1	1	1	2276.2276	2276.2276	0.0000
4	1	1	3	0	2276.2408	2276.2407	0.0001
3	2	1	2	1	2276.3020	2276.3018	0.0002
5	1	1	4	0	2276.3150	2276.3148	0.0002
9	4	1	9	3	2276.3481	2276.3479	0.0002
9	4	1	9	3	2276.3481	2276.3479	0.0002

J'	K'	L'	J''	K''	Observed	Calculated	Obs.-Calc.
8	4	1	8	3	2276.3481	2276.3480	0.0001
8	4	1	8	3	2276.3481	2276.3480	0.0001
7	4	1	7	3	2276.3481	2276.3482	0.0000
7	4	1	7	3	2276.3481	2276.3482	0.0000
6	4	1	6	3	2276.3481	2276.3483	-0.0001
6	4	1	6	3	2276.3481	2276.3483	-0.0001
5	4	1	5	3	2276.3481	2276.3484	-0.0003
5	4	1	5	3	2276.3481	2276.3484	-0.0003
6	1	1	5	0	2276.3890	2276.3889	0.0001
3	3	1	2	2	2276.4370	2276.4367	0.0003
5	2	1	4	1	2276.4501	2276.4500	0.0001
4	3	1	3	2	2276.5110	2276.5108	0.0002
6	2	1	5	1	2276.5241	2276.5241	0.0000
8	1	1	7	0	2276.5372	2276.5370	0.0001
7	2	1	6	1	2276.5981	2276.5981	0.0000
4	4	1	3	3	2276.6456	2276.6453	0.0003
4	4	1	3	3	2276.6456	2276.6453	0.0003
6	3	1	5	2	2276.6592	2276.6589	0.0002
8	2	1	7	1	2276.6718	2276.6722	-0.0005
5	4	1	4	3	2276.7196	2276.7194	0.0002
5	4	1	4	3	2276.7196	2276.7194	0.0002
7	3	1	6	2	2276.7329	2276.7330	-0.0001
11	7	1	11	6	2276.7493	2276.7491	0.0003
11	7	1	11	6	2276.7493	2276.7491	0.0003
10	7	1	10	6	2276.7493	2276.7492	0.0002
10	7	1	10	6	2276.7493	2276.7492	0.0002
9	7	1	9	6	2276.7493	2276.7494	0.0000
9	7	1	9	6	2276.7493	2276.7494	0.0000
8	7	1	8	6	2276.7493	2276.7496	-0.0002
8	7	1	8	6	2276.7493	2276.7496	-0.0002
7	7	1	7	6	2276.7493	2276.7498	-0.0004
7	7	1	7	6	2276.7493	2276.7498	-0.0004
8	3	1	7	2	2276.8067	2276.8070	-0.0004
5	5	1	4	4	2276.8541	2276.8536	0.0005
7	4	1	6	3	2276.8677	2276.8675	0.0002
7	4	1	6	3	2276.8677	2276.8675	0.0002

J'	K'	L'	J''	K''	Observed	Calculated	Obs.-Calc.
6	5	1	5	4	2276.9279	2276.9276	0.0002
8	4	1	7	3	2276.9413	2276.9415	-0.0002
8	4	1	7	3	2276.9413	2276.9415	-0.0002
10	3	1	9	2	2276.9543	2276.9551	-0.0008
4	3	-1	5	4	2287.7860	2287.7864	-0.0004
7	1	-1	8	2	2287.7860	2287.7873	-0.0013
3	3	-1	4	4	2287.8613	2287.8605	0.0008
6	1	-1	7	2	2287.8613	2287.8614	-0.0001
4	2	-1	5	3	2287.8983	2287.8981	0.0002
4	2	-1	5	3	2287.8983	2287.8981	0.0002
7	0		8	1	2287.8983	2287.8988	-0.0005
3	2	-1	4	3	2287.9722	2287.9722	0.0000
3	2	-1	4	3	2287.9722	2287.9722	0.0000
6	0		7	1	2287.9722	2287.9729	-0.0007
4	1	-1	5	2	2288.0094	2288.0097	-0.0002
7	1	1	8	0	2288.0094	2288.0103	-0.0008
5	4	-1	5	5	2288.0462	2288.0456	0.0006
6	4	-1	6	5	2288.0462	2288.0457	0.0005
7	4	-1	7	5	2288.0462	2288.0458	0.0004
8	4	-1	8	5	2288.0462	2288.0459	0.0003
9	4	-1	9	5	2288.0462	2288.0461	0.0001
10	4	-1	10	5	2288.0462	2288.0463	-0.0001
2	2	-1	3	3	2288.0462	2288.0464	-0.0002
2	2	-1	3	3	2288.0462	2288.0464	-0.0002
5	0		6	1	2288.0462	2288.0471	-0.0009
8	2	1	9	1	2288.0462	2288.0476	-0.0014
3	1	-1	4	2	2288.0837	2288.0839	-0.0002
6	1	1	7	0	2288.0837	2288.0844	-0.0008
4	3	-1	4	4	2288.1573	2288.1573	0.0000
5	3	-1	5	4	2288.1573	2288.1574	-0.0001
6	3	-1	6	4	2288.1573	2288.1574	-0.0001
7	3	-1	7	4	2288.1573	2288.1575	-0.0002
8	3	-1	8	4	2288.1573	2288.1576	-0.0003
9	3	-1	9	4	2288.1573	2288.1578	-0.0005
10	3	-1	10	4	2288.1573	2288.1580	-0.0007
2	1	-1	3	2	2288.1573	2288.1581	-0.0008

J'	K'	L'	J''	K''	Observed	Calculated	Obs.-Calc.
5	1	1	6	0	2288.1573	2288.1586	-0.0013
1	1	-1	2	2	2288.2324	2288.2323	0.0002
4	1	1	5	0	2288.2324	2288.2328	-0.0003
4	2	-1	4	3	2288.2685	2288.2690	-0.0005
4	2	-1	4	3	2288.2685	2288.2690	-0.0005
5	2	-1	5	3	2288.2685	2288.2691	-0.0005
5	2	-1	5	3	2288.2685	2288.2691	-0.0005
6	2	-1	6	3	2288.2685	2288.2691	-0.0006
6	2	-1	6	3	2288.2685	2288.2691	-0.0006
7	2	-1	7	3	2288.2685	2288.2692	-0.0006
7	2	-1	7	3	2288.2685	2288.2692	-0.0006
8	2	-1	8	3	2288.2685	2288.2693	-0.0007
2	0		3	1	2288.2685	2288.2696	-0.0011
2	1	-1	2	2	2288.3810	2288.3807	0.0004
3	1	-1	3	2	2288.3810	2288.3807	0.0003
4	1	-1	4	2	2288.3810	2288.3807	0.0003
5	1	-1	5	2	2288.3810	2288.3807	0.0003
6	1	-1	6	2	2288.3810	2288.3807	0.0003
7	1	-1	7	2	2288.3810	2288.3808	0.0003
8	1	-1	8	2	2288.3810	2288.3809	0.0002
9	1	-1	9	2	2288.3810	2288.3810	0.0001
10	1	-1	10	2	2288.3810	2288.3811	-0.0001
2	1	1	3	0	2288.3810	2288.3812	-0.0001
4	0		4	1	2288.4927	2288.4923	0.0005
3	0		3	1	2288.4927	2288.4923	0.0005
5	0		5	1	2288.4927	2288.4923	0.0005
2	0		2	1	2288.4927	2288.4923	0.0005
1	0		1	1	2288.4927	2288.4923	0.0005
6	0		6	1	2288.4927	2288.4923	0.0005
7	0		7	1	2288.4927	2288.4923	0.0004
8	0		8	1	2288.4927	2288.4924	0.0004
9	0		9	1	2288.4927	2288.4925	0.0003
10	0		10	1	2288.4927	2288.4926	0.0002
5	1	1	5	0	2288.6040	2288.6038	0.0002
6	1	1	6	0	2288.6040	2288.6038	0.0002
4	1	1	4	0	2288.6040	2288.6038	0.0002

J'	K'	L'	J''	K''	Observed	Calculated	Obs.-Calc.
3	1	1	3	0	2288.6040	2288.6038	0.0002
7	1	1	7	0	2288.6040	2288.6038	0.0002
2	1	1	2	0	2288.6040	2288.6038	0.0002
1	1	1	1	0	2288.6040	2288.6038	0.0002
8	1	1	8	0	2288.6040	2288.6038	0.0002
9	1	1	9	0	2288.6040	2288.6039	0.0001
10	1	1	10	0	2288.6040	2288.6040	0.0000
3	0		2	1	2288.7154	2288.7149	0.0005
6	2	1	6	1	2288.7154	2288.7152	0.0002
5	2	1	5	1	2288.7154	2288.7152	0.0002
7	2	1	7	1	2288.7154	2288.7152	0.0002
4	2	1	4	1	2288.7154	2288.7152	0.0001
3	2	1	3	1	2288.7154	2288.7153	0.0001
8	2	1	8	1	2288.7154	2288.7153	0.0001
2	2	1	2	1	2288.7154	2288.7153	0.0001
9	2	1	9	1	2288.7154	2288.7153	0.0001
10	2	1	10	1	2288.7154	2288.7154	0.0000
6	1	-1	5	2	2288.8264	2288.8259	0.0005
3	1	1	2	0	2288.8264	2288.8264	0.0000
7	3	1	7	2	2288.8264	2288.8266	-0.0002
6	3	1	6	2	2288.8264	2288.8266	-0.0002
5	3	1	5	2	2288.8264	2288.8266	-0.0002
8	3	1	8	2	2288.8264	2288.8266	-0.0002
4	3	1	4	2	2288.8264	2288.8266	-0.0002
3	3	1	3	2	2288.8264	2288.8267	-0.0002
9	3	1	9	2	2288.8264	2288.8267	-0.0002
10	3	1	10	2	2288.8264	2288.8267	-0.0003
5	0		4	1	2288.8637	2288.8633	0.0004
2	2	1	1	1	2288.8637	2288.8637	0.0000
10	3	-1	9	4	2288.9003	2288.8996	0.0007
7	1	-1	6	2	2288.9003	2288.9001	0.0002
4	1	1	3	0	2288.9003	2288.9006	-0.0003
6	0		5	1	2288.9380	2288.9375	0.0005
3	2	1	2	1	2288.9380	2288.9379	0.0001
7	4	1	7	3	2288.9380	2288.9379	0.0001
7	4	1	7	3	2288.9380	2288.9379	0.0001

J'	K'	L'	J''	K''	Observed	Calculated	Obs.-Calc.
6	4	1	6	3	2288.9380	2288.9379	0.0001
6	4	1	6	3	2288.9380	2288.9379	0.0001
5	4	1	5	3	2288.9380	2288.9379	0.0000
5	4	1	5	3	2288.9380	2288.9379	0.0000
8	1	-1	7	2	2288.9749	2288.9744	0.0005
5	1	1	4	0	2288.9749	2288.9748	0.0001
7	0		6	1	2289.0121	2289.0117	0.0004
4	2	1	3	1	2289.0121	2289.0121	0.0001
9	1	-1	8	2	2289.0493	2289.0486	0.0007
6	1	1	5	0	2289.0493	2289.0490	0.0003
7	5	1	7	4	2289.0493	2289.0492	0.0001
8	5	1	8	4	2289.0493	2289.0492	0.0001
6	5	1	6	4	2289.0493	2289.0492	0.0001
9	5	1	9	4	2289.0493	2289.0492	0.0001
10	5	1	10	4	2289.0493	2289.0492	0.0000
3	3	1	2	2	2289.0493	2289.0493	0.0000
11	5	1	11	4	2289.0493	2289.0493	-0.0001
12	5	1	12	4	2289.0493	2289.0495	-0.0002
8	0		7	1	2289.0865	2289.0859	0.0005
5	2	1	4	1	2289.0865	2289.0863	0.0002
10	1	-1	9	2	2289.1237	2289.1228	0.0009
7	1	1	6	0	2289.1237	2289.1232	0.0005
4	3	1	3	2	2289.1237	2289.1235	0.0003
10	0		9	1	2289.2350	2289.2344	0.0006
7	2	1	6	1	2289.2350	2289.2346	0.0004
4	4	1	3	3	2289.2350	2289.2348	0.0003
4	4	1	3	3	2289.2350	2289.2348	0.0003
9	1	1	8	0	2289.2716	2289.2716	0.0000
6	3	1	5	2	2289.2716	2289.2718	-0.0002
11	0		10	1	2289.3089	2289.3086	0.0003
8	2	1	7	1	2289.3089	2289.3088	0.0002
5	4	1	4	3	2289.3089	2289.3089	0.0000
5	4	1	4	3	2289.3089	2289.3089	0.0000
10	1	1	9	0	2289.3465	2289.3458	0.0007
7	3	1	6	2	2289.3465	2289.3459	0.0005
9	8	1	9	7	2289.3829	2289.3826	0.0003

J'	K'	L'	J''	K''	Observed	Calculated	Obs.-Calc.
10	8	1	10	7	2289.3829	2289.3826	0.0002
11	8	1	11	7	2289.3829	2289.3827	0.0001
12	8	1	12	7	2289.3829	2289.3829	0.0000
12	0		11	1	2289.3829	2289.3829	-0.0001
9	2	1	8	1	2289.3829	2289.3830	-0.0001
6	4	1	5	3	2289.3829	2289.3831	-0.0002
6	4	1	5	3	2289.3829	2289.3831	-0.0002
11	1	1	10	0	2289.4201	2289.4201	0.0000
8	3	1	7	2	2289.4201	2289.4201	0.0000
5	5	1	4	4	2289.4201	2289.4201	-0.0001
8	4	1	7	3	2289.5317	2289.5314	0.0003
8	4	1	7	3	2289.5317	2289.5314	0.0003
11	2	1	10	1	2289.5317	2289.5314	0.0002
14	0		13	1	2289.5317	2289.5317	0.0000
7	5	1	6	4	2289.5678	2289.5684	-0.0006
10	3	1	9	2	2289.5678	2289.5685	-0.0007
6	6	1	5	5	2289.6050	2289.6054	-0.0004
9	4	1	8	3	2289.6050	2289.6055	-0.0005
9	4	1	8	3	2289.6050	2289.6055	-0.0005
12	2	1	11	1	2289.6050	2289.6057	-0.0006

Appendix B

Supplementary data for Chapter 4

Trimer Complexes

Calculated and observed transitions for C_6D_6–He_2, C_6D_6–Ne_2 and C_6D_6–Ar_2 trimers.

Table B.1: Observed transitions in the $\nu_2 + \nu_{13}$ ($\sim$ 2275 cm^{-1}) and ν_{12} ($\sim$ 2288 cm^{-1}) bands of C_6D_6–He_2.

J'	K'	L'	J''	K''	Observed	Calculated	Obs.-Calc.
2	2	1	1	1	2276.4713	2276.4714	-0.0001
3	3	1	2	2	2276.6808	2276.6809	-0.0001
4	4	1	3	3	2276.8899	2276.8900	-0.0001
0	0		1	1	2275.8915	2275.8911	0.0004
1	0		2	1	2275.7311	2275.7308	0.0003
1	1	-1	2	2	2275.6804	2275.6805	-0.0002
2	1	-1	3	2	2275.5200	2275.5202	-0.0002
2	2	-1	3	3	2275.4695	2275.4696	-0.0000
2	2	-1	3	3	2275.4695	2275.4696	-0.0000
4	1	1	3	0	2276.7409	2276.7405	0.0004
5	2	1	4	1	2276.9493	2276.9491	0.0002
2	1	1	3	0	2275.6204	2275.6206	-0.0002
3	2	-1	4	3	2275.3089	2275.3092	-0.0003
3	3	-1	4	4	2275.2586	2275.2582	0.0004
4	3	-1	5	4	2275.0973	2275.0977	-0.0004
4	4	-1	5	5	2275.0465	2275.0464	0.0001
5	5	1	4	4	2277.0988	2277.0987	0.0001

J'	K'	L'	J''	K''	Observed	Calculated	Obs.-Calc.
6	3	1	5	2	2277.1567	2277.1569	-0.0002
3	0		2	1	2276.5307	2276.5312	-0.0005
4	1	-1	5	2	2275.2000	2275.1996	0.0003
1	1	1	0	0	2288.9163	2288.9163	0.0000
2	2	1	1	1	2289.1022	2289.1021	0.0001
3	1	1	2	0	2289.2360	2289.2365	-0.0005
3	2	1	2	1	2289.2619	2289.2619	0.0000
3	3	1	2	2	2289.2880	2289.2879	0.0001
4	2	1	3	1	2289.4215	2289.4215	-0.0000
4	3	1	3	2	2289.4472	2289.4475	-0.0003
4	4	1	3	3	2289.4735	2289.4735	-0.0000
0	0		1	1	2288.5700	2288.5699	0.0001
1	0		2	1	2288.4097	2288.4095	0.0002
1	1	-1	2	2	2288.3835	2288.3835	-0.0000
2	1	1	3	0	2288.2752	2288.2755	-0.0003
2	0		3	1	2288.2493	2288.2493	0.0001
2	1	-1	3	2	2288.2233	2288.2232	0.0001
2	2	-1	3	3	2288.1968	2288.1971	-0.0003
3	1	-1	4	2	2288.0630	2288.0630	-0.0000
3	3	-1	4	4	2288.0104	2288.0104	-0.0000
5	3	1	4	2	2289.6070	2289.6068	0.0002
5	4	1	4	3	2289.6323	2289.6329	-0.0006
5	5	1	4	4	2289.6592	2289.6590	0.0002
3	2	-1	4	3	2288.0368	2288.0368	0.0001
4	3	-1	5	4	2287.8502	2287.8501	0.0001

J'	K'	L'	J''	K''	Observed	Calculated	Obs.-Calc.
4	4	-1	5	5	2287.8235	2287.8235	-0.0000
6	2	1	5	1	2289.7396	2289.7397	-0.0001
6	3	1	5	2	2289.7661	2289.7658	0.0004
6	4	1	5	3	2289.7918	2289.7920	-0.0001
6	5	1	5	4	2289.8182	2289.8181	0.0001
6	6	1	5	5	2289.8444	2289.8443	0.0001
1	1	1	2	0	2288.4356	2288.4355	0.0001
2	0		1	1	2289.0505	2289.0503	0.0002
3	0		2	1	2289.2101	2289.2100	0.0001
5	2	1	4	1	2289.5810	2289.5807	0.0003
7	4	1	6	3	2289.9505	2289.9507	-0.0001
8	8	1	7	7	2290.2144	2290.2144	-0.0000

Table B.2: Observed transitions in the $\nu_2 + \nu_{13}$ and ν_{12} bands of C_6D_6–Ne_2.

J'	K'	L'	J''	K''	Observed	Calculated	Obs.-Calc.
5	1	1	4	0	2276.2080	2276.2078	0.0002
2	1	1	1	0	2276.0357	2276.0353	0.0004
1	0		2	1	2275.6540	2275.6540	0.0000
2	0		3	1	2275.5956	2275.5961	-0.0005
4	0		5	1	2275.4795	2275.4796	-0.0001
6	2	1	5	1	2276.4174	2276.4178	-0.0004
3	3	1	2	2	2276.3898	2276.3897	0.0002
4	3	1	3	2	2276.4502	2276.4504	-0.0002
3	1	1	4	0	2275.6883	2275.6887	-0.0003
4	1	1	5	0	2275.6310	2275.6306	0.0004
2	1	-1	3	2	2275.4436	2275.4436	-0.0001
3	1	-1	4	2	2275.3859	2275.3858	0.0001
6	3	1	5	2	2276.5731	2276.5728	0.0003
5	4	1	4	3	2276.6638	2276.6638	0.0000
4	4	1	3	3	2276.5991	2276.5992	-0.0001
6	4	1	5	3	2276.7293	2276.7292	0.0000
2	2	-1	3	3	2275.2891	2275.2889	0.0002
5	5	1	4	4	2276.8162	2276.8163	-0.0001
9	7	1	8	6	2277.4840	2277.4840	-0.0000
4	2	-1	5	3	2275.1752	2275.1752	0.0000
5	1	-1	6	2	2275.2691	2275.2692	-0.0002
1	1	1	0	0	2288.7485	2288.7485	0.0001
3	1	1	2	0	2288.8643	2288.8645	-0.0002
1	0		2	1	2288.4467	2288.4468	-0.0001

J'	K'	L'	J''	K''	Observed	Calculated	Obs.-Calc.
3	0		4	1	2288.3312	2288.3312	-0.0000
2	1	-1	3	2	2288.2608	2288.2606	0.0002
5	2	-1	6	3	2287.9591	2287.9592	-0.0000
3	3	-1	4	4	2287.9457	2287.9458	-0.0001
4	1	-1	5	2	2288.1457	2288.1452	0.0005
3	2	1	2	1	2288.9918	2288.9921	-0.0003
6	1	1	5	0	2289.0414	2289.0410	0.0004
3	3	1	2	2	2289.1202	2289.1202	0.0000
4	3	1	3	2	2289.1779	2289.1780	-0.0000
4	4	1	3	3	2289.3059	2289.3057	0.0001
6	4	1	5	3	2289.4214	2289.4218	-0.0003
5	5	1	4	4	2289.4913	2289.4909	0.0004
5	3	1	4	2	2289.2356	2289.2360	-0.0004
3	1	1	4	0	2288.4602	2288.4600	0.0002
6	3	-1	7	4	2287.7728	2287.7730	-0.0002
4	4	-1	5	5	2287.7587	2287.7590	-0.0002
5	4	-1	6	5	2287.7011	2287.7011	0.0000
7	4	-1	8	5	2287.5866	2287.5865	0.0001
6	6	-1	7	7	2287.3837	2287.3836	0.0001
7	5	1	6	4	2289.6071	2289.6071	-0.0000

Table B.3: Observed transitions in the $\nu_2 + \nu_{13}$ and ν_{12} bands of C_6D_6–Ar_2.

J'	K'	L'	J''	K''	Observed	Calculated	Obs.-Calc.
2	2	1	1	1	2276.1465	2276.1463	0.0002
3	2	1	2	1	2276.1759	2276.1759	-0.0000
3	3	1	2	2	2276.3532	2276.3533	-0.0001
4	3	1	3	2	2276.3826	2276.3828	-0.0003
3	1	1	4	0	2275.7895	2275.7899	-0.0004
4	1	1	5	0	2275.7602	2275.7599	0.0002
6	1	1	7	0	2275.7005	2275.6998	0.0007
3	0		4	1	2275.6118	2275.6117	0.0001
4	0		5	1	2275.5822	2275.5818	0.0004
2	1	-1	3	2	2275.4632	2275.4630	0.0002
5	3	1	4	2	2276.4125	2276.4123	0.0002
8	3	1	7	2	2276.5010	2276.5008	0.0002
9	3	1	8	2	2276.5307	2276.5303	0.0003
10	3	1	9	2	2276.5599	2276.5600	-0.0001
11	3	1	10	2	2276.5888	2276.5897	-0.0008
8	4	1	7	3	2276.6769	2276.6772	-0.0003
9	4	1	8	3	2276.7066	2276.7066	0.0000
7	5	1	6	4	2276.8239	2276.8239	-0.0001
6	6	1	5	5	2276.9708	2276.9706	0.0002
7	2	1	7	1	2276.0855	2276.0857	-0.0002
6	2	1	6	1	2276.0855	2276.0860	-0.0005
8	2	1	8	1	2276.0855	2276.0853	0.0002
6	1	1	6	0	2275.9080	2275.9083	-0.0004
8	1	1	8	0	2275.9080	2275.9078	0.0001

J'	K'	L'	J''	K''	Observed	Calculated	Obs.-Calc.
6	0		6	1	2275.7302	2275.7303	-0.0001
7	0		7	1	2275.7302	2275.7301	0.0001
7	1	-1	7	2	2275.5518	2275.5517	0.0001
6	1	-1	6	2	2275.5518	2275.5518	0.0000
8	3	-1	8	4	2275.1937	2275.1937	0.0000
7	3	-1	7	4	2275.1937	2275.1937	-0.0000
9	3	-1	9	4	2275.1937	2275.1937	0.0000
6	3	-1	6	4	2275.1937	2275.1937	-0.0000
10	3	-1	10	4	2275.1937	2275.1937	0.0000
11	3	-1	11	4	2275.1937	2275.1937	-0.0000
5	3	-1	5	4	2275.1937	2275.1938	-0.0001
4	3	-1	4	4	2275.1937	2275.1938	-0.0001
10	2	1	9	1	2288.8847	2288.8847	-0.0001
3	1	1	2	0	2288.5187	2288.5188	-0.0000
1	1	1	0	0	2288.4590	2288.4585	0.0004
2	0		3	1	2288.1844	2288.1842	0.0002
1	0		2	1	2288.2133	2288.2136	-0.0003
0	0		1	1	2288.2430	2288.2431	-0.0001
4	1	1	5	0	2288.2814	2288.2813	0.0001
3	1	1	4	0	2288.3105	2288.3106	-0.0002
2	2	1	1	1	2288.6461	2288.6457	0.0004
4	2	1	3	1	2288.7056	2288.7058	-0.0002
9	2	1	8	1	2288.8557	2288.8555	0.0002
3	3	1	2	2	2288.8334	2288.8339	-0.0005
8	3	1	7	2	2288.9814	2288.9813	0.0001

J'	K'	L'	J''	K''	Observed	Calculated	Obs.-Calc.
4	4	1	3	3	2289.0225	2289.0225	-0.0000
7	4	1	6	3	2289.1089	2289.1089	0.0000
9	4	1	8	3	2289.1648	2289.1648	0.0001
10	4	1	9	3	2289.1919	2289.1919	-0.0001
5	5	1	4	4	2289.2108	2289.2107	0.0000
8	5	1	7	4	2289.2932	2289.2930	0.0002
9	5	1	8	4	2289.3191	2289.3193	-0.0002
7	2	1	6	1	2288.7960	2288.7960	0.0001
6	1	-1	7	2	2287.9125	2287.9129	-0.0004
3	2	-1	4	3	2287.8475	2287.8474	0.0001
6	2	-1	7	3	2287.7594	2287.7593	0.0001